Journal of the Meteorological Society of Japan

EARLY ONLINE RELEASE

Size-resolved Aerosol Microphysics in a Global Nonhydrostatic Atmospheric Model: Model Description and Validation

Chiu Tung CHENG[1]

and

Kentaroh SUZUKI

Atmosphere and Ocean Research Institute
The University of Tokyo, Kashiwa, Japan

1 April, 2020

----

1) Corresponding author: ChiuTung Cheng, Atmosphere and Ocean Research Institute, the University of Tokyo, Kashiwa Research Complex, 5-1-5, Kashiwanoha, Kashiwa, Chiba Prefecture 277-8568 JAPAN

Email: ctcheng@aori.u-tokyo.ac.jp

Tel: +81-070-4074-9295

1

Abstract

The transport and removal processes of aerosol particles, as well as their potential impacts on clouds and climate, are strongly dependent on the particle sizes. Recent advances in computational capabilities enable us to develop sectional aerosol schemes for general circulation models and chemical transport models. The sectional aerosol modeling framework provides a capacity to explicitly simulate the variations in size distributions due to microphysical processes such as nucleation and coagulation, based on the mechanisms suggested from laboratory studies and field observations. Here, we develop a two-moment sectional aerosol scheme for Spectral Radiation-Transport Model for Aerosol Species (SPRINTARS-bin) for use in NICAM (Nonhydrostatic ICosahedral Atmospheric Model) as an alternative to the original mass-based (single-moment) SPRINTARS-orig aerosol module. NICAM-SPRINTARS is a seamless multiscale model that has been used for regional-to-global simulations of different resolutions based on the same model framework. In this study, we performed global simulations with NICAM-SPRINTARS-bin at typical climate model resolution ($\Delta x \sim 230km$) with nudging to a meteorological re-analysis. We compared our results with equivalent simulations for the original model (NICAM-SPRINTARS-orig) and observations including 500nm aerosol optical depth and 440-870nm Angstrom Exponent in AErosol RObotic NETwork (AERONET) measurements, particle number concentrations measured at Global Atmospheric Watch (GAW) sites and size-resolved number concentrations measured at European Supersites for Atmospheric Aerosol Research (EUSAAR) and German Ultrafine Aerosol Network (GUAN) sites. We found that compared to NICAM-SPRINTARS-orig, NICAM-SPRINTARS-bin demonstrates the long-range transport of ultra-fine particles to high latitudes and predicts higher Angstrom Exponent and total number concentrations that better agrees with observations. The latter underscores the importance of resolving the microphysical processes that determine concentrations of ultra-fine aerosol particles and explicitly represent size-dependent deposition in predicting these properties. However, number concentrations of coarse particles are still underestimated by both the original mass-based and the new microphysical schemes. Further efforts are needed to understand the reasons for the differences with the observed size distributions, including testing different emission and secondary organic aerosol production schemes, incorporating inter-species

2

57 coagulation and black carbon aging, as well as performing simulations with higher

58 spatial resolutions.

59 **Keywords**   NICAM-SPRINTARS; aerosol; microphysics; sectional scheme;

60

1   Introduction

Atmospheric aerosols perturb the global energy budget directly by scattering and absorbing incoming shortwave radiation (Haywood & Boucher, 2000) and indirectly through interactions with clouds (Lohmann & Feichter, 2005; Fan *et al.*, 2016). The magnitudes of both aerosol-radiation and aerosol-cloud radiative effects are strongly dependent on the size distributions of aerosol particles. For example, the mass scattering efficiency of visible light usually has a maximum in the accumulation mode (with particle diameters between 0.1 and 1 µm) of the aerosol population. Aerosols can also act as cloud condensation nuclei (CCN), forming cloud droplets and affecting the albedo and lifetime of clouds (Boucher *et al.*, 2013). Due to the weaker Kelvin effect and stronger solute effect, larger particles exhibit lower critical supersaturations and are more likely to be activated. The number concentration of CCN is usually defined as the number of particles with a dry diameter greater than 50 or 100 nm (e.g., Asmi et al., 2011), although the exact threshold diameter also depends on the aerosol hygroscopicity, supersaturation of the ambient air, and updraft velocity.

To the first approximation, the size distributions of aerosols can be represented by multiple log-normal distributions, each "mode" representing a different source of particles (see Whitby, 1978). However, changes in dust size distributions caused by preferential deposition during transport have been observed (Maring *et al.*, 2003; Van Der Does *et al.*, 2016), illustrating the limitations in constraining the particle size distributions using fixed modal radii and widths even for particles from the same emission source.

84   In global aerosol models, the aerosol size distributions are mostly represented by

85   two different approaches: the modal approach and the sectional approach. The

86   modal approach can be further divided into 1-moment and 2-moment schemes

87   (Textor *et al.*, 2006; Mann *et al.*, 2014). The 1-moment modal scheme (often referred

88   to as the bulk approach) tracks only the aerosol mass concentrations, with the size

89   distributions being prescribed for each of several aerosol types. In contrast, in the 2-

90   moment modal scheme (e.g., GLOMAP-mode: Mann et al., 2010), both the aerosol

91   mass and number are transported among several size classes. This allows the size

92   distributions to vary both spatially and temporally through the effect of aerosol

93   microphysical processes, including coagulation and condensation.

94   The sectional approach models the particle size distributions explicitly,

95   discretizing them into several size bins (sections). The evolution of size distributions

96   is then driven by the size-dependent properties of each size bin, such as the terminal

97   velocities and collision efficiencies. Different size resolutions are chosen in different

98   sectional global aerosol microphysics models, ranging from 10 bins (Bergman *et al.*,

99   2012) and 12 bins (Gong & Barrie, 2003) to higher resolutions of 20 bins (Spracklen

100   *et al.*, 2005) and 30 bins (Adams & Seinfeld, 2002). At the expense of requiring a

101   larger investment of computation times, the sectional schemes produce more

102   realistic simulations compared to the modal approach (Zhang *et al.*, 2002;

103   Weisenstein *et al.*, 2007), and the sectional aerosol models with a large number of

104   bins are often considered as the "true value" for tuning the modal scheme (e.g.,

105   Mann *et al.*, 2012). The sectional approach can be considered as representing the

106   size distribution explicitly. It allows to fully resolve the size dependence of aerosol

107   emission and removal processes and in the representations of microphysical

108   processes such as nucleation, condensation, and coagulation. New theories or

mechanisms are proposed to explain the field observations (e.g., new particle formation events, severe haze events, and size distributions of primary aerosols), and a size-resolving scheme is the essential building block to incorporate the new knowledge realistically from experimental and field studies into the aerosol model.

Several sectional aerosol modules have been developed and applied in chemical transport models (CTMs) and general circulation models (GCMs). They included CAM (Gong *et al.*, 2003), GLOMAP-bin (Spracklen *et al.*, 2005), APM (Yu & Luo, 2009), TOMAS (Adams & Seinfeld, 2002; Lee & Adams, 2012), and SALSA (Kokkola *et al.*, 2008, 2018; Bergman *et al.*, 2012). Higher-dimensional sectional schemes have also been developed. For instance, ATRAS uses a two-dimensional sectional scheme to resolve both the particle size and aerosol mixing state (Matsui *et al.*, 2014; Matsui, 2017; Matsui & Mahowald, 2017). Ching *et al.* (2016) developed a three-dimensional sectional representation scheme (MOSAIC-mix) to additionally resolve the hygroscopicity.

The aerosol transport model SPRINTARS (Takemura *et al.*, 2000) uses a hybrid approach. More specifically, sulfate and carbonaceous aerosols are treated using the bulk scheme, whereas mineral dust and sea spray are simulated using the sectional approach, with the size distributions represented using 10 and 4 bins, respectively. The SPRINTARS model has been implemented in the Nonhydrostatic ICosahedral Atmospheric Model (NICAM, Satoh *et al.*, 2014). It has been used for multiscale global simulations, including those with the finest horizontal resolution of 870 m (Miyamoto *et al.*, 2013). This aerosol-coupled version of NICAM, called NICAM-SPRINTARS (Suzuki *et al.*, 2008), includes both aerosol-cloud and aerosol-radiation interactions and has been used for simulations with global-to-regional scales and low-to-high resolutions. For example, Dai et al. (2018) ran the model as a

6

134   GCM with a horizontal resolution of 223 km and evaluated the climatology of the dust

135   cycle. Goto et al. (2019) used NICAM-SPRINTARS for regional simulations, with the

136   highest resolution of 11 km over Japan. The model has successfully captured the

137   aerosol plume from Siberian wildfires as observed by two geostationary satellites

138   (Himawari-8 and COMS). Goto et al. (2018) performed month-long global high-

139   resolution (~10 km) simulations in different seasons, and the simulated global

140   distributions of aerosol optical depth were comparable to those observed by MODIS

141   and AERONET.

142   In this study, we describe a two-moment sectional scheme for SPRINTARS,

143   coded such that a variable number of size bins can be specified for each aerosol

144   type. In this case, aerosol microphysical processes are coupled to radiative transfer

145   and cloud processes, with subsequent dynamical processes, within the framework of

146   NICAM. Simulations are performed at a typical climate model's resolution of ~200 km,

147   but as NICAM-SPRINTARS is a seamless global-to-regional model, the same size-

148   resolving aerosol model can also be used with higher resolutions in future studies. In

149   the following sections, we first introduce NICAM-SPRINTARS and the settings used

150   for the simulations in this study (Section 2), followed by the descriptions of the

151   aerosol microphysical scheme SPRINTARS-bin and its implementation into NICAM

152   as NICAM-SPRINTARS-bin (Section 3). Results from year-2006 nudged simulations

153   with NICAM-SPRINTARS-bin simulations are compared to observations, and an

154   equivalent NICAM-SPRINTARS-orig run in Section 4. In Section 5, we discuss the

155   ways to improve the model-observation discrepancies and the possibilities enabled

156   by using the size-resolving scheme in NICAM-SPRINTARS.

157

2 Model descriptions and experiment settings

2.1 Global cloud-resolving model NICAM

As the first global cloud-resolving model (Satoh *et al.*, 2008, 2019), NICAM is based on a non-hydrostatic dynamic core (Tomita & Satoh, 2004). It has been used for global simulations with flexible horizontal resolutions varying from conventional climate model resolutions (e.g., Dai *et al.*, 2018; Goto *et al.*, 2018) to grid spacings of kilometer-scale (Tomita *et al.*, 2005; Miura *et al.*, 2007; Suzuki *et al.*, 2008) or smaller than one kilometer (Miyamoto *et al.*, 2013). In the high-resolution experiments, NICAM resolves deep convection and considers cloud microphysical models without the use of cumulus parameterizations that have led to fundamental uncertainties in conventional GCMs (Stevens & Bony, 2013). By resolving the multiscale cloud structures, NICAM has been used for studies of tropical cyclones and Madden Julian Oscillations (Miura *et al.*, 2007). It can also be used as a regional model with a stretch-grid system (Uchida *et al.*, 2016) and a limited-domain grid configuration (Uchida *et al.*, 2017), in which the target area is resolved by higher resolutions with a relatively low computational cost. The same model has also been used to conduct long-term simulations for climate studies (e.g., Kodama *et al.*, 2015).

To validate the size-resolved model and consistently compare its results with the original NICAM-SPRINTARS model, we performed simulations with a horizontal grid resolution of 223 km and a time step of 20 minutes. A large-scale condensation scheme is used for cloud formation processes. As Dai et al. (2018) indicated the importance of meteorological nudging on aerosol transport simulations, we nudged the model with temperatures and wind speeds in 6-hour intervals with the NCEP Final (FNL) Operational Global Analysis data (NOAA/NCEP, 2000). The simulations were performed from July 2005 to December 2006, with the first six months regarded

183   as a spin-up period due to the zero aerosol concentrations assumed initially. The

184   year 2006 was chosen for simulations in alignment with the other size-resolved

185   model simulations evaluated in an AeroCom paper (Mann *et al.*, 2014) as well as in

186   previous NICAM-SPRINTARS simulations (Suzuki *et al.*, 2008; Dai *et al.*, 2018). Two

187   experiments have been performed with identical settings, except that one of them

188   uses the original SPRINTARS model, and the other employs the size-resolved model

189   developed in this study. Hereafter, we denote the original model as SPRINTARS-orig,

190   the size-resolving model as SPRINTARS-bin, and use SPRINTARS when referring

191   to the SPRINTARS model in general.

192   2.2 Aerosol model SPRINTARS

193   The aerosol model SPRINTARS treats the emission, vertical mixing, wet and dry

194   depositions of aerosols, while the aerosol tracer transport is handled by the host

195   model. SPRINTARS was originally developed for use in a conventional GCM: the

196   Model for Interdisciplinary Research on Climate (MIROC). To simulate aerosols with

197   higher resolution, Suzuki et al. (2008) implemented SPRINTARS into NICAM and

198   simulated the effect of aerosols on warm clouds using a horizontal grid spacing of 7

199   km globally. The global simulation was able to reproduce the aerosol-dependencies

200   of liquid water path and vertical growth of cloud droplets as observed by satellites.

201   To date, NICAM-SPRINTARS has been used for global simulations with horizontal

202   resolutions ranging from 10 to 230 km (Suzuki *et al.*, 2008; Goto *et al.*, 2018, 2020;

203   Sato *et al.*, 2018) as well as regional simulations with a resolution of ~10 km over

204   Japan (Goto *et al.*, 2015, 2019).

205   SPRINTARS considers four aerosol types, the total aerosols consisting of an

206   external mixture of sea salt, soil dust, sulfate, and carbonaceous aerosols. In

207   SPRINTARS-orig, the particle size distribution is represented using the sectional or

208   modal approach depending on the aerosol type as follows.

209   Sea salt and soil dust are coarse particles emitted from natural sources, and their

210   emission strengths are calculated online based primarily on local wind speed

211   (Section 3.3). The mixing ratios of salt and dust are tracked by 4 and 10 size bins,

212   respectively. Each bin represents a population of particles with the same predefined

213   diameter, and the deposition fluxes are calculated according to the particle size.

214   Sulfate aerosol (ammonium sulfate) is produced from the oxidation of SO_2 and

215   dimethylsulfide (DMS) with O_3, H_2O_2, and OH radicals (Takemura *et al.*, 2000). The

216   particle number distribution is assumed to follow a log-normal distribution with a dry

217   mode diameter of 139 nm (d'Almeida *et al.*, 1991). Hygroscopic growth of particles is

218   considered when calculating the terminal velocities and mass extinction coefficients.

219   Similarly, the size distributions of carbonaceous aerosols are assumed log-normal,

220   with different mode diameters and standard deviations depending on the sub-types.

221   These include black carbon (BC), organic carbon (OC), and biogenic secondary

222   organic aerosols (BSOA). The mode diameters and standard deviations follow the

223   values used in Goto *et al.* (2020) and are listed in Table 1.

224   In the simulations, we used the year 2010 emission inventories of HTAP-v2.2

225   (Janssens-Maenhout *et al.*, 2015) for anthropogenic emissions of SO_2, OC, and BC.

226   For emissions from biomass burning, the average emissions from 2005 to 2014 of

227   the Global Fire Emissions Database (GFED, https://www.globalfiredata.org/) are

228   used. The year 2000-2009 averages of the AeroCom-HC (Diehl *et al.*, 2012) are

229   used for volcanic SO_2 emissions. The emission inventories of isoprene and terpene

230   from the Global Emissions InitiAtive (GEIA) are used as the sources of secondary

231   organic aerosols.

232   The emission fluxes of DMS are calculated online as a function of downward

233   surface solar flux (Bates *et al.*, 1987). The same three-dimensional profiles of

234   oxidants (O_3, H_2O_2, and OH radicals) as in Takemura *et al.* (2005) are used, which

235   are generated from a climate run targeted for the 2000s using a global chemical

236   transport model (CHASER) coupled to MIROC (Sudo *et al.*, 2002).

237   **3   Sectional aerosol microphysical module: SPRINTARS-bin**

238   The sectional version of SPRINTARS introduced in this study (SPRINTARS-bin)

239   is built upon the current framework of SPRINTARS-orig. The size distributions of all

240   aerosol types are discretized into a flexible number of size bins, and aerosol

241   microphysical processes are simulated with consideration of aerosol sizes. Here,

242   only the size-dependent components of each process are described, and readers

243   may refer to Takemura et al. (2000) for detailed descriptions and formulation of

244   SPRINTARS.

245   3.1 Definitions of size bins

246   In SPRINTARS-bin, each external mixture of aerosol species is divided into

247   several size bins. The number of bins and the overall size range of the size

248   distributions are flexible so that they can be adjusted depending on the

249   computational resources available (see Table S1 for the computational times using a

250   range of bin numbers). In this study, the number of bins for each size distribution is

251   set to 20, which is well above the minimum numbers obtained from sensitivity tests in

252   other sectional models (e.g., Foret et al., 2006; Gong et al., 2003; Lee and Adams,

253 2012). The size ranges of dust and salt are the same as in the SPRINTARS-orig,

254 whereas the diameters of sulfate and carbonaceous aerosols span over 3 nm - 10

255 µm and 80 nm - 5 µm ranges, respectively (Table 1).

256   The boundaries of size bins are equally spaced in the logarithmic scale, and the

257 initial bin center of each size bin is defined as the mid-point of the boundaries. The

258 "bin center" represents the dry diameter of all particles that belong to the size

259 category and is used for the online calculation of size-dependent properties. Bin

260 centers are modified according to the moving center scheme (Jacobson, 1997a) to

261 represent the particle growth due to microphysics, including condensation and

262 coagulation.

263 3.2 Hygroscopic growth

264   For hygroscopic aerosols (sulfate, sea salt, and OC), the wet diameters (d_{wet})

265 are calculated from the dry particle diameters (d_{dry}) using the following empirical

266 power-law relation to estimate the growth factor, fitted using the values reported in

267 d'Almeida *et al.* (1991) :

268 $$d_{wet} = \begin{cases} d_{dry} & , \ RH < RH_c \\ d_{dry} * c_{gf}(1 - RH)^{\gamma_{gf}} & , \ RH \geq RH_c \end{cases} \quad (1)$$

269   Here RH and RH_c are the ambient and crystallization relative humidity,

270 respectively. Moreover, c_{gf} and γ_{gf} are the growth factor parameters (see Table S2

271 in supplementary material). The wet volumes are used for the calculation of

272 coagulation between particles, as well as computing the aerosol properties, including

273 terminal velocities, collision efficiencies with raindrops, and mass extinction

274 efficiencies.

3.3 Source functions

SPRINTARS-bin adopts the same emission flux calculation schemes for sea salt and soil dust as in SPRINTARS-orig (Takemura *et al.*, 2000). The emission flux of sea salt depends on the wind speed at 10 m above the surface, whereas the emission flux of soil dust is a function of wind speed and soil moisture. The freshly emitted particles are assumed to follow a given size distribution, namely the source function. Many source functions have been proposed based on *in situ* measurements or laboratory experiments (e.g., Alfaro & Gomes, 2001; Kok, 2011a, 2011b; Schulz et al., 1998 for soil dust; Gong, 2003; Monahan et al., 1986 for sea salt). In both the original and sectional models, the source function proposed in Monahan et al. (1986) is used for sea salt, while the interpolation of results in d'Almeida & Schütz (1983) is used as the source function of soil dust. It should be noted that the choice of source functions affects the aerosol properties and can be an important source of model uncertainties. The source functions used in this study are selected for consistency in comparison with SPRINTARS-orig, although the sensitivity to different source functions should be investigated in future studies.

Emission strengths of carbonaceous aerosols are determined by the emission inventories. Unlike dust and sea salt, source function parameterizations are not proposed for primary carbonaceous aerosols, and the initial size distributions are assumed to follow the same log-normal distributions as in SPRINTARS-orig (Table 1). After emission, the size distributions are modified by the subsequent differential removal processes. In principle, the size distribution of BSOA should be computed by explicitly simulating the aerosol dynamical processes (Section 3.4). BSOA precursor gases are oxidized in the atmosphere, forming low-volatility species that condense on existing particles such as sulfate and BC. However, the current

300 SPRINTARS model does not resolve the chemical evolutions of organic volatile

301 gases and does not consider internal mixtures of different aerosol types (e.g.,

302 sulfate-OC mixtures). In SPRINTARS-bin, a simple approach is taken by specifying

303 constant fractions of the isoprene and terpene emission fluxes to form pure organic

304 particles immediately after the emission. The initial size distribution of these BSOA

305 particles is assumed to follow the log-normal distribution with the same mode

306 diameter and standard deviation as in SPRINTARS-orig (Table 1).

307 3.4 Aerosol dynamics

308 In SPRINTARS, the production of sulfuric acid is calculated from the major

309 oxidation pathways of the emitted SO_2 and DMS. The sulfuric acid is then combined

310 with atmospheric ammonia to form ammonium sulfate. SPRINTARS-orig assumes

311 that all produced sulfates are particles forming immediately at the assumed size

312 distribution. In contrast, SPRINTARS-bin explicitly considers the gas-to-particle

313 conversion and subsequent particle growth processes of ammonium sulfate, i.e.,

314 new   particle   formation   (nucleation   and   post-nucleation   growth),

315 condensation/evaporation, and coagulation.

316 The first step to convert gas to particles is the nucleation of stabilized clusters.

317 The model calculates the nucleation rates and diameters based on the binary

318 homogenous nucleation theory. Given the gas-phase sulfuric acid concentrations,

319 temperature, and relative humidity, the nucleation rates and critical cluster diameters

320 are calculated using a recently developed parameterization scheme (Määttänen *et*

321 *al.*, 2018), which can be considered as an updated and generalized version of the

322 binary nucleation parameterizations commonly used in other sectional models

323 (Kulmala *et al.*, 1998; Vehkamäki *et al.*, 2002). The parameterization scheme also

324 provides the calculation of ion-induced nucleation, but it is not considered in this

325 study due to the lack of information on atmospheric ions in the current model. The

326 nucleation rates in the first layer are calculated using activation-type nucleation

327 theory (Kulmala *et al.,* 2006) because the binary nucleation theory often does not

328 reproduce the observed nucleation rates in the boundary layer. The theory is

329 proposed based on atmospheric observations and suggests an empirical formula

330 that relates the nucleation rates of 1 nm clusters to the gas phase sulfuric acid

331 concentrations.

332 The typical diameters of freshly nucleated particles are around 1 nm, while the

333 detection limits of the instruments used in most field measurements are larger than 3

334 nm. To reduce the computational cost of the post-nucleation growth to detectable

335 sizes, the "apparent" formation rate is calculated from the "real" nucleation rate by

336 comparing the condensation growth rate with the scavenging rate due to coagulation

337 with background aerosols (Kerminen & Kulmala, 2002; Lehtinen *et al.*, 2007). Self-

338 coagulation of the freshly nucleated particles is calculated using the scheme

339 proposed by Anttila et al. (2010).

340 The coagulation kernel is calculated as the sum of kernels resulting from the

341 following processes (Jacobson, 2005): Brownian diffusion and convective Brownian

342 diffusion enhancement, gravitational collection, turbulent inertial motion, and

343 turbulent shear. The semi-implicit coagulation scheme (Jacobson *et al.*, 1994) is

344 used to solve the coagulation of particles larger than 3 nm in the same-size

345 distribution. As different types of aerosols are treated as external mixtures in

346 SPRINTARS, only the coagulation among internally mixed particles is taken into

347 account.

348　　　The condensational growth of aerosol particles is solved using the analytical

349　predictor of condensation (APC) scheme (Jacobson, 1997b), which serves as a non-

350　iterative and unconditionally stable solution to the growth equation. For simplicity,

351　only one type of condensing species (sulfuric acid) is considered, and the water

352　content in sulfate particles is calculated according to the hygroscopic growth relation

353　(Section 3.2). The vapor pressure of sulfuric acid is calculated from the ambient

354　temperature. Marti et al. (1997) suggested that the presence of even a few

355　ammonium ions can effectively stabilize the sulfuric acid clusters and lower the vapor

356　pressures. In SPRINTARS-bin, we assume the ubiquitous presence of ammonium

357　ions in the atmosphere and use the relation from Marti *et al.* (1997) to calculate

358　vapor pressure.

359　3.5 Deposition

360　　　The overall deposition flux is the sum of mass fluxes due to wet deposition, dry

361　deposition, and gravitational settling. The differential deposition fluxes of different

362　size bins are mainly driven by the terminal velocities, which depend on the particle

363　size, temperature as well as air density. The terminal velocities are then used to

364　calculate the rates of dry deposition, gravitational settling as well as sub-cloud

365　scavenging processes.

366　a.　Wet deposition

367　　　Wet removal of aerosols can be divided into two parts: sub-cloud and in-cloud

368　scavenging. The re-emission of aerosols from the evaporation of raindrops is also

369　considered. The number concentration of particles scavenged due to collision with

370　raindrops ($\triangle N_{ar}$) is calculated from equation (A5) in Takemura et al., (2000):

371 $$\triangle N_{ar} = E\pi(r_r + r_a)^2(v_r - v_a)N_r N_a \qquad (2)$$

372 where E is the collision efficiency between aerosol particles and raindrops. Here r, v,

373 and N stand for the radii, terminal velocities, and number concentrations,

374 respectively, while subscripts r and a correspond to raindrops and aerosols. The

375 raindrop radius is assumed to be 0.5 mm. In principle, the collision efficiency can

376 also be calculated online, given the aerosol size and raindrop size spectrum.

377 However, detailed microphysics of clouds and precipitation are not explicitly

378 represented in this study. Therefore, to a first approximation, the collision efficiency

379 of each size bin is assumed to be constant during the simulation.

380   In-cloud scavenging is the removal of aerosols from cloud water by precipitation.

381 Aerosols can also be re-emitted from the evaporated raindrops. The key quantity to

382 determine is the amount of aerosols in the precipitation. The ratios of aerosols

383 dissolved in water are defined as the in-cloud coefficients C_{in}. In SPRINTARS-orig,

384 C_{in} for sulfate and sea salt are assumed to be 0.8, OC to be 0.4, dust and BC to be

385 0.1 (the "SIMPLE" scheme). When aerosol-cloud interactions are concerned, C_{in} can

386 also be calculated online using the activation schemes (Abdul-Razzak *et al.*, 1998;

387 Abdul-Razzak & Ghan, 2000). Regardless of the scheme, a bulk C_{in} value is

388 obtained for each aerosol type, and the same mass fraction is removed for any size

389 (Fig. 1).

390   On the other hand, in-cloud scavenging in SPRINTARS-bin is size-dependent.

391 The size distribution is divided into two parts according to the activation diameter d_{act}.

392 Only the particles with a diameter larger than d_{act} are subject to in-cloud scavenging.

393 The activation diameter can be inferred from the assumed C_{in} in the "SIMPLE"

394 scheme, or calculated using the activation scheme (the "ABDUL02" scheme). It was

395 developed for sectional representation (Abdul-Razzak & Ghan, 2002) and can be

396 integrated into the scheme developed for multiple aerosol types (Abdul-Razzak &

397 Ghan, 2000).

398   The purpose of this study is to investigate the fundamental behavior of different

399 size representations. Therefore, the same constant in-cloud coefficients are used for

400 both SPRINTARS-orig and SPRINTARS-bin models to minimize the possible

401 feedback due to aerosol-cloud interactions. To diagnose CCN properties of the

402 simulated size distributions under the meteorological conditions, the values C_{in} and

403 d_{act} are calculated from the aerosol size distributions and meteorological conditions

404 using the "ABDUL02" scheme (discussed in Section 5) but not used in the

405 simulations.

406 b.   Dry deposition

407   Both SPRINTARS-orig and SPRINTARS-bin models use the same scheme for

408 calculating the dry deposition fluxes (Takemura *et al.*, 2000). The overall dry

409 deposition velocity is dependent on the aerodynamical resistance and quasi-laminar

410 resistance. The aerodynamical resistance is provided by the host model (NICAM),

411 whereas the values of quasi-laminar resistance are fixed for sulfate and

412 carbonaceous aerosols in SPRINTARS-orig. In SPRINTARS-bin, the latter is

413 calculated online as a function of terminal velocities and friction velocities provided

414 by NICAM. For gravitational settling, the mass fluxes are proportional to the terminal

415 velocities.

416

417

418   3.6 Optical properties

419   To evaluate the single-wavelength aerosol optical thickness, the optical

420   parameters, including the mass extinction coefficients and mass absorption

421   coefficients, are calculated from Mie theory. The refractive indices (Table S3) used

422   for calculations are set to values used by other SPRINTARS simulations (Takemura

423   *et al.*, 2003; Goto *et al.*, 2011, 2015). In SPRINTARS-orig, the parameters are

424   averaged over the prescribed size distribution. The same approach is also used to

425   calculate the optical properties for each size bin of dust and sea salt. In

426   SPRINTARS-bin, the parameters of each size bin are calculated exactly at the bin

427   center, assuming all particles in the size bin have the same diameter. As a result, the

428   aerosol optical properties can be analyzed in relation to the predicted variations in

429   size distributions (Fig. 2).

430   **4   Results**

431   Here we present results from NICAM-SPRINTARS-orig, NICAM-SPRINTARS-bin,

432   and   NCEP-reanalysis-nudged   simulations   representative   of   the   year   2006

433   (emissions   and   meteorology).   We focus on the global distributions of aerosols,

434   including the mass and number concentrations, as well as optical properties. We

435   then compare the results with *in situ* and remote sensing aerosol measurements to

436   validate the simulation results against observations.

437   4.1 Spatial distributions of aerosols

438   a.   Mass concentrations

439   Global maps of the annual-mean surface mass concentrations of each aerosol

440   type are shown in Fig. 3 for NICAM-SPRINTARS-orig and NICAM-SPRINTARS-bin,

441 and the zonally-averaged vertical mass concentrations are shown in Fig. 4. In

442 general, different representations of aerosol size distributions do not lead to

443 significant differences in surface mass concentrations. This is not surprising because

444 the same emission inventories or schemes are used, and the meteorological

445 variables are nudged. The observed differences may be attributed to the sensitivities

446 of removal fluxes to the underlying size distributions.

447 The largest aerosol burden at the surface is contributed by soil dust, with the

448 highest surface concentrations over the Sahara desert and East Asia (Figs. 3a and

449 3b). The distributions are similar for both simulations. The emission of dust from

450 deserts in the northern hemisphere explains the peak observed in the zonal-mean

451 vertical profiles (Figs. 4a and 4b). The emitted soil dust is lifted to the troposphere,

452 and the highest concentrations are found above 0.8 km from the surface. Values

453 higher than 0.5 µg m^{-3} can be found at the upper troposphere (~10 km). A small

454 peak can also be observed near the 20S due to dust emitted from deserts in

455 Argentina, South Africa, and Australia. The highest values are found at heights over

456 0.5 km. The overall patterns of the vertical profiles predicted by the two models are

457 similar, but NICAM-SPRINTARS-bin predicts a slightly stronger vertical transport

458 (Fig. 4b).

459 Sea salt is abundant in the Pacific and Atlantic oceans, but high concentrations

460 are also found in the Arctic (Figs. 3c and 3d) because of the extremely high wind

461 speed (> 14 m s^{-1}) predicted in the region. The overall patterns of the results are

462 similar, but NICAM-SPRINTARS-bin produces higher surface concentrations. The

463 similarities of results from the two models suggest that an increase in the number of

464 size bins does not exert a critical influence on mass concentrations with the same

465 source functions. The vertical transport of sea salt is weaker than that of soil dust,

466 with the highest concentrations of sea salt found at the boundary layer.

467   The highest concentrations of sulfate aerosols are found over China, the Middle

468 East and, eastern North America (Figs. 3e and 3f) due to anthropogenic emissions.

469 Although both models show similar peaks in these regions, the two models show

470 different characteristics of aerosol transport. In NICAM-SPRINTARS-orig, the

471 extents of poleward transport are similar in the two hemispheres. Concentrations

472 below 0.05 µg m^{-3} are predicted at latitudes above around 60° (northern hemisphere)

473 and 45° (southern hemisphere). In contrast, NICAM-SPRINTARS-bin shows a

474 stronger transport of sulfate mass in the northern hemisphere than in the southern

475 hemisphere. Concentrations above 0.1 µg m^{-3} are simulated in the Arctic region,

476 whereas concentrations lower than 0.05 µg m^{-3} are predicted in the sub-tropical

477 oceans in the southern hemisphere. Different model behaviors are also identified in

478 vertical profiles of the meridional mean (Figs. 4e and 4f). This can be attributed to

479 different terminal velocities of particles in different size bins, which are not resolved

480 in NICAM-SPRINTARS-orig. With the lower terminal velocities and longer lifetimes,

481 smaller particles can be transported to the upper levels and regions away from

482 sources.

483   The surface concentrations of BC and OC are shown in Figs. 3g-j. Both

484 subtypes of carbonaceous aerosols are abundant in South Africa due to biomass

485 burning and over Asia due to primary carbon emissions from industrial sources or

486 isoprene emissions from vegetation. The surface mass concentrations of BC are

487 also substantial over the United States, whereas the OC concentrations are

488 relatively high over the northern part of South America. Only small differences are

489 observed when comparing the results of the two models.

490   In contrast to the prescribed size distribution in NICAM-SPRINTARS-orig, the

491   sizes of sulfate in NICAM-SPRINTARS-bin are determined by aerosol microphysics

492   (Section 3.4), with additional effects due to transport, chemistry, and removal

493   processes. All four of these types of processes can cause substantially different size

494   distributions. For carbonaceous aerosols, the initial size distributions are assumed to

495   be the same as in NICAM-SPRINTARS-orig, and the size-dependent deposition

496   processes may not largely alter the size distributions, resulting in overall similar

497   patterns of surface concentrations and vertical mass profiles.

498   b.   Number concentrations

499   The number concentration is an important quantity for aerosols. It is often

500   measured in the field and serves as the primary aerosol metric for the strength of

501   aerosol-cloud interactions. Figures 5 and 6 show the surface and zonal-mean

502   vertical profiles of number concentrations of different aerosol types, respectively.

503   Given similar surface mass concentrations between the two models for all aerosol

504   types in Fig. 3, the contrasting patterns of surface number concentrations predicted

505   by the two models are attributed to different underlying size distributions. The

506   surface number concentrations shown are divided into four size classes according to

507   the dry diameters: 3-30 nm, 30-50 nm, 50-100 nm, and above 100 nm. The number

508   concentration in each size class is calculated by considering the bin centers for the

509   aerosol types represented in size bins. For sulfate and carbonaceous aerosols in

510   NICAM-SPRINTARS-orig, the number concentrations are calculated from assumed

511   log-normal number size distributions at fixed dry mode diameters and standard

512   deviations.

513   NICAM-SPRINTARS-orig predicts that most of the aerosol particles have dry

514   diameters above 50 nm (Figs. 5e and 5g), which can be explained assuming that dry

515   mode diameters of these aerosols are larger than 100 nm (Table 1). While the total

516   surface mass burden is mostly contributed by soil dust (Figs. 3a and 3b), the highest

517   values in number concentrations can be found in regions where sulfate aerosol is

518   abundant (Fig. 3c). As the mode diameters and thus the size distributions are fixed in

519   SPRINTARS-orig, the number concentrations are mostly determined by the sulfate

520   mass concentrations.

521   In NICAM-SPRINTARS-bin, high values of number concentrations are found

522   over the regions where fine mode aerosols are abundant. For example, values of

523   over 1000 cm^{-3} are found over East Asia and South Asia, where industrial emission

524   of sulfate and carbonaceous aerosols are substantial. The peaks found over central

525   Africa can be attributed to the OC and BC emitted from biomass burning. High

526   number concentrations exceeding 5000 cm^{-3} are found over eastern North America

527   due to the abundance of sulfate aerosol. Over South America, the number

528   concentrations exhibit a peak in Columbia and Brazil due to the abundance of

529   organic carbon, particularly BSOA originated from isoprene.

530   Long-range transport mostly occurs for the finest particles. Particles with

531   diameters smaller than 30 nm are transported to distant oceans, leading to

532   concentrations in the range of 100 to 500 cm^{-3} found over most of the oceans. The

533   number concentrations of particles in these regions are lower for coarser particles.

534   The number concentrations of particles with diameters between 30 to 50 nm over the

535   southern Pacific Ocean are below 100 cm^{-3} (Figure 5d), and the upper limit further

536   decreases to 50 cm^{-3} for particles with diameters greater than 50 nm (Figures 5f and

537   5h). Number concentrations higher than 100 cm^{-3} are predicted over the central part

23

538 of the Pacific Ocean, which is distant from the continents, but the values are mostly

539 lower than 50 cm^{-3} for larger particles (Figure 5h).

540   The finest particles are also transported to high latitudes. The number

541 concentrations above 100 cm^{-3} of particle diameter below 30 nm are found over the

542 Arctic and above 50 cm^{-3} over Antarctica. The values in the Arctic are substantially

543 higher than those in Antarctica owing to the proximity of the sulfate sources region.

544 The number concentrations in Antarctica decrease to about 10 cm^{-3} for particles with

545 diameters between 50 to 100 nm. In contrast, the particle number concentrations

546 simulated by NICAM-SPRINTARS-orig in these regions are always below 10 cm^{-3} for

547 any size categories.

548   To investigate the zonal-means at different altitudes (Fig. 6), the size class above

549 100 nm is further divided into three classes: 100-700 nm, 700-1000 nm, and above

550 1000 nm (1 μm). The results of both models show that the number concentrations of

551 particles with diameters larger than 700 nm are substantially lower than those

552 between 100 to 700 nm. Consistent with number concentrations, the surface mass

553 in NICAM-SPRINTARS-orig shows peak values in the 50-100 nm and 100-700 nm

554 size classes, and the vertical profile patterns in these size classes are similar to that

555 of sulfate mass concentrations (Fig. 4e). In contrast, NICAM-SPRINTARS-bin

556 predicts the highest number concentrations in the 3-30 nm size class. High number

557 concentrations are found over the tropics at above 12 km, with values greater than

558 500 cm^{-3}. The relatively low mass concentrations and high number concentrations

559 indicate the small particle sizes. This may be attributed to low temperatures in the

560 upper troposphere that may inhibit coagulation, which is a major sink of fine particles

561 and a source of larger particles. For coarser particles (700-1000 nm and above 1000

562 nm, Figs. 6e and 6f), the vertical profiles are similar for both size classes, in contrast

24

563   to the much lower concentration in the 700-1000 nm class simulated in NICAM-

564   SPRINTARS-orig.

565   c.   Optical properties

566   The aerosol optical depths (AOD) and Angstrom Exponent (AE) simulated by the

567   models are presented in Fig. 7. Similar to the surface mass concentrations (Fig. 3),

568   the spatial patterns of AOD simulated by both models do not show large differences

569   as AOD mainly reflects the aerosol burden. The patterns mostly follow the

570   distributions of soil dust, which contributes to the largest mass burdens among all

571   aerosol types. However, it can be observed that AODs in the Middle East and

572   northern China are slightly lower in NICAM-SPRINTARS-bin. These regions are

573   usually associated with the abundance of sulfate aerosols (sulfate AOD). As shown

574   in Fig. 4, NICAM-SPRINTARS-bin predicts similar sulfate masses in the whole

575   column, so the differences in sulfate AOD is not due to lower mass burden. As

576   SPRINTARS-bin considers the size-dependencies of the optical properties (Fig. 2),

577   the lower AODs indicate that the simulated size distribution peak at particle sizes

578   with weaker interactions with radiation. As discussed in Section 5.2, this may be

579   associated with the internal mixing processes with other aerosol types not simulated

580   in the current model.

581   The Angstrom Exponent in the model is calculated using the following equation:

582    $$AE = -\log\left(\frac{AOD_{\lambda_1}}{AOD_{\lambda_2}}\right)/\log(\frac{\lambda_1}{\lambda_2}) \quad (3)$$

583   where AOD_{λ_i} is the AOD at the wavelength of λ_i. In this study, λ_1 and λ_2 are chosen

584   to be 870 and 440 nm, respectively. AE reflects the spectral dependence of the

585   optical depth on wavelengths and is used as a quantity to evaluate the particle sizes,

586   as the extinction efficiencies of fine particles are more sensitive to the wavelengths in

587   this range.

588   Comparing the AE simulated by the two models, NICAM-SPRINTARS-bin

589   generally predicts higher values, which are consistent with the smaller particle sizes

590   as discussed in Section 4.1b. Values above 1.8 are simulated over the northern

591   parts of Russia and North America and can be explained by the transport of the

592   finest particles to these regions (Fig. 5b). The distributions of AOD and AE will be

593   discussed in more detail in Section 4.2d in comparison with observations from

594   MODIS.

595   4.2 Comparisons with measurements

596   a.   Comparisons of surface mass concentrations with IMPROVE

597   We compared the annually-averaged surface mass concentrations (Fig. 3) with

598   the year 2006 data from the IMPROVE program (United States Interagency

599   Monitoring of Protected Visual Environment; http://vista.cira.colostate.edu/improve).

600   All stations are located in North America, and only the masses of fine particles

601   (diameter < 2.5 µm) are considered. Figure 8 shows the scatter plots of the model

602   results against IMPROVE measurements for four aerosol types: sea salt, sulfate, BC,

603   and OC. As listed in Table 2, the model-observation correlations for sea salt are 0.68

604   and 0.70 for NICAM-SPRINTARS-orig and NICAM-SPRINTARS-bin, respectively. At

605   the same time, the scatter plot (Fig. 8a) suggests that the surface sea salt masses

606   are overestimated at 165 (NICAM-SPRINTARS-orig) and 169 (NICAM-SPRINTARS-

607   bin) of the 170 stations, and NICAM-SPRINTARS-bin generally predicts higher

608   values. This may be attributed to the fact that the emission of sea salt is sensitive to

609   the wind speed that is not well resolved in the low horizontal resolution used in this

26

610 study. On the other hand, the surface sulfate mass concentrations at the stations

611 exhibit reasonable correlation coefficients (0.73 and 0.65 for NICAM-SPRINTARS-

612 orig and NICAM-SPRINTARS-bin) but tend to be underestimated in both models (Fig.

613 8b). The correlation coefficients for BC (0.45) and OC (0.53) are lower. Both models

614 underestimate the surface masses, and NICAM-SPRINTARS-bin predicts a smaller

615 bias than NICAM-SPRINTARS-orig. Overall, both models reproduce the variations in

616 surface mass concentrations in North America fairly well.

617 b.   Surface number concentrations with GAW

618   Following the previous model evaluation for global aerosol microphysics models

619 (Bergman *et al.*, 2012; Mann *et al.*, 2014), we compared the simulated surface

620 number concentrations with observations at 12 stations of GAW (Global Atmosphere

621 Watch; https://community.wmo.int/activity-areas/gaw) that have a long measurement

622 time series from Condensation Nucleus Counter (CNC) deployed at the station (for

623 at least 15 years). Figure 9 shows the annual averages of the models plotted against

624 the annual mean of the multi-year measurements with error bars showing the

625 interannual variability. The total number concentrations from the models are

626 calculated as the total number of particles above the threshold diameter specified by

627 the particular CNC used at each station. It should be noted that the logarithmic scale

628 is used for plotting and computing the statistics as the particle concentrations vary

629 across several orders of magnitude.

630   The results indicate that NICAM-SPRINTARS-orig underestimates the total

631 number concentrations at most of the stations: the values are underestimated by

632 more than one order of magnitude at half of the stations. This can be attributed to the

633 limitations of NICAM-SPRINTARS-orig in predicting the number concentration of fine

634   particles, which usually dominates the total number concentrations. On the other

635   hand, NICAM-SPRINTARS-bin tends to predict higher number concentrations of fine

636   particles relative to coarse particles (Fig. 5). The model can reproduce the observed

637   values within one order of magnitude at 11 out of the 12 stations. Figure 10

638   compares the monthly averages of number concentrations observed at GAW

639   stations and simulated by the models. It is evident that NICAM-SPRINTARS-bin

640   predicts values closer to observations at most of the stations, with NICAM-

641   SPRINTARS-orig underestimating the number concentrations by more than an order

642   of magnitude at several stations (e.g., Barrow, South Pole). The seasonal variations

643   are also fairly well captured by NICAM-SPRINTARS-bin at some of the stations (e.g.,

644   Pallas, Neumayer). The size-resolving capacity of NICAM-SPRINTARS-bin thus

645   greatly improves over the strong underprediction of total number concentrations

646   predicted by NICAM-SPRINTARS-orig.

647   c.   Size-resolved number concentrations in Europe (EUSAAR)

648   The EUSAAR (European Supersites for Atmospheric Aerosol Research;

649   http://www.eusaar.net/) project provides harmonized aerosol measurement data from

650   European field monitoring stations (Philippin *et al.*, 2009). Asmi et al. (2011)

651   analyzed the measured size-resolved number concentrations during 2008-09 and

652   provided a convenient dataset for comparisons with models. In this study, we

653   compare the model results with the surface number concentrations (Fig. 11) in three

654   size classes defined by the dry diameter: between 30 and 50 nm (N30-50), larger

655   than 50 nm (N50), and larger than 100 nm (N100). For the finest particles (N30-50),

656   NICAM-SPRINTARS-orig   underestimates   the   annually-averaged   number

657   concentrations at all stations: the values of 23 out of the 24 stations are lower than

658   10^{-1} of the observed values. On the other hand, NICAM-SPRINTARS-bin produces

659 values closer to those observed, with values at 22 out of 24 stations within one order

660 of magnitude of the observations (Fig. 11a). For the coarser particles (N50 and

661 N100), the number concentrations simulated by both models are closer to

662 observations than N30-50. The number concentrations of N50 predicted by NICAM-

663 SPRINTARS-orig and NICAM-SPRINTARS-bin are within one order of magnitude of

664 the observed values at 9 and 19 stations, but most of the values are underestimated.

665 For N100, both models underestimate the number concentrations at all stations. The

666 underestimated number concentrations of coarse particles may imply fewer potential

667 CCN predicted in both models given the relevance of coarse particles to CCN

668 (Andreae & Rosenfeld, 2008).

669 d. Optical properties: AOD and AE

670   To investigate the column-integrated optical properties of aerosols, we compare

671 the model-simulated AOD and AE with two observational datasets from remote-

672 sensing measurements: AERONET and MODIS. AERONET (AErosol RObotic

673 NETwork) routinely provides quality-assured retrievals of AOD and AE from ground-

674 based sky radiance measurements (Holben *et al.*, 1998) and is often used for

675 validation or calibration of satellite-retrieved aerosol products. We use the Level 2

676 daily average product to calculate the annual averages for the 144 stations with

677 more than 100 days of valid data in the year 2006. To evaluate the global distribution

678 of aerosol properties, we also calculate the annual average at each grid point using

679 the Collection 6.1 Level 3 monthly products of AOD and AE (Platnick *et al.*, 2015)

680 measured by MODIS (Moderate Resolution Imaging Spectroradiometer). Wei *et al.*

681 (2019) evaluated the performance of MODIS/Terra and MODIS/Aqua Collection 6.1

682 monthly AOD and found that neither instrument consistently outperforms the other

683 over land. To increase the reliability of the comparisons to the satellite aerosol

684 measurements, we compared the model results to the mean of the aerosol optical

685 depths values from the two instruments.

686   The AODs predicted by both models at the AERONET stations are similar at

687 most of the stations (Fig. 12a). The AODs predicted by NICAM-SPRINTARS-bin at

688 over 93% of the stations are within 0.5 to 2 times of the values predicted by NICAM-

689 SPRINTARS-orig. This is consistent with the similar mass concentrations simulated

690 in the models (Figs. 3 and 4). The different AODs can also be attributed to

691 differences in underlying size distributions and the ways to calculate extinction

692 coefficients. The aerosol masses at most of the stations are dominated by soil dust.

693 It is also treated with the sectional method in SPRINTARS-orig, which explains why

694 the two models produce similar values of AOD. Both models give high correlations

695 with the AERONET-observed values and small negative bias, with a higher

696 correlation simulated by NICAM-SPRINTARS-orig (0.65 vs. 0.64) but smaller bias by

697 NICAM-SPRINTARS-bin (-0.16 vs. -0.04).

698   On the other hand, the Angstrom Exponent (AE) simulated at the stations exhibit

699 very different behaviors in the two models. NICAM-SPRINTARS-orig underestimates

700 the AE at most of the stations, and the correlation coefficient is 0.29. The

701 underestimation of AE by NICAM-SPRINTARS-orig is also reported in a previous

702 study (Dai *et al.*, 2014). This suggests that SPRINTARS-orig tends to overestimate

703 the particle sizes, as the finest particles are removed at the same rate as the larger

704 ones in the bulk scheme. The correlation coefficient increased to 0.45 by resolving

705 the size and aerosol microphysics in NICAM-SPRINTARS-bin. The annual averages

706 of AE still tend to be underestimated but to a smaller extent. Overall, NICAM-

707 SPRINTARS-bin gives better agreement for this size-relevant metric.

708   The annual means of AOD and AE observed by MODIS are shown in Figs. 7a

709   and 7d. High AOD (~0.6) are observed over North Africa, accompanied by low AE

710   (<0.6). This can be explained by the emission of coarse soil dust particles from the

711   Sahara desert. Similar results in this region are also reproduced by both NICAM-

712   SPRINTARS-orig and NICAM-SPRINTARS-bin. The soil dust is transported across

713   the Atlantic Ocean, creating a low AE belt near the equator. Both models predict the

714   westward transport of soil dust, but the belt is not apparent over the ocean. In

715   MODIS, the high AOD region extends westward and reaches the Caribbean Sea, but

716   those simulated by both models are shifted northward. Biomass burning in Central

717   Africa explains the AOD peak (~0.5) as well as the high AE (>1.5) in the southern

718   part of Africa, as observed by MODIS. The models also simulate the AOD peak in

719   central Africa, but AE in the southern part of Africa is lower than the values observed

720   by MODIS.

721   The high AOD values over China observed by MODIS are suggested to be

722   contributed by both soil dust from deserts and anthropogenic emissions from

723   industrial areas (Luo *et al.*, 2014). The high AE (above 1.2) observed in this region

724   suggests that it is dominated by fine particles, including sulfate and carbonaceous

725   aerosols. Both models simulate the AOD peak in China, but the AE is

726   underestimated, and the values are similar to those over the Sahara Desert. The

727   model-predicted AOD peaks are dominated by the presence of soil dust, and the

728   contributions of aerosols from anthropogenic emissions are not well captured by the

729   models.

730   In general, both models predict lower AOD in the industrial regions. For example,

731   AOD and AE peaks are observed over the Middle East, India, and near Brazil by

732   MODIS, but the models tend to underestimate the peak values, with NICAM-

31

733 SPRINTARS-bin predicting lower values. The AE is also underestimated, but
734 NICAM-SPRINTARS-bin gives values that are closer to the observations. The
735 model-observation discrepancy may be explained by the limitations of the coarse
736 grid resolution in mapping the emission inventories. The underestimation may also
737 be partly attributed to the missing contribution of nitrate-containing aerosols, as
738 suggested in previous studies using the SPRINTARS model (Dai *et al.*, 2018; Park *et*
739 *al.*, 2018). The aging of BC by the condensation and coagulation by non-BC species
740 are not simulated in the model, which may also lead to underestimated AOD at
741 regions away from the BC sources.

742   The MODIS analysis suggests that the AOD over most of the oceans is lower
743 than 0.2, but peaks with values up to 0.4 are simulated by the models. This may
744 indicate that the sea salt burden may be overestimated, as positive bias is found in
745 the sea salt mass concentrations at the IMPROVE stations. Values higher than 0.4
746 are observed by MODIS over the East China Sea, Sea of Japan, and the Sea of
747 Okhotsk. The models also reproduce this high AOD region and suggest that the
748 major contribution is from soil dust transported from China. The observed AE is
749 about 0.9-1.2 in these regions, and NICAM-SPRINTARS-bin simulates closer values
750 to observations compared to NICAM-SPRINTARS-orig. At high-latitude regions,
751 including Russia and Canada, NICAM-SPRINTARS-bin predicts very high values of
752 AE (>1.8) due to the long-range transport of fine particles, which is not observed by
753 MODIS.

754 **5   Discussions**

755   In general, the results from NICAM-SPRINTARS-bin are in reasonable
756 agreement with the benchmark *in situ* and remote sensing aerosol observations that

757 have been used to evaluate global aerosol microphysics models (e.g., Mann *et al.*,

758 2014). In particular, the comparisons show that NICAM-SPRINTARS-bin improves

759 the prediction of quantities that are more relevant to aerosol sizes, including the

760 number concentration and Angstrom Exponent. It implies that the underlying size

761 distributions are better captured by NICAM-SPRINTARS-bin. The size information

762 from the size-resolving models may also be useful for other physical processes, such

763 as the total surface area for chemical reactions in the chemistry module, the size-

764 dependent optical properties for the radiation scheme, and the number concentration

765 of CCN for cloud microphysics.

766   We acknowledge that the use of a size-resolving aerosol model alone is not

767 sufficient to produce size distributions as observed in the field. The introduction of a

768 size-resolving scheme in this study should be viewed as a framework that enables

769 the implementations and testing of different parameters of aerosol properties and

770 microphysics schemes suggested from observations and experiments. Thus, it is

771 important to discuss potential factors that may affect the predicted size distributions

772 and thus should be considered in future studies.

773 5.1 Choices of model parameters and emission schemes

774   This study focuses on the sensitivity of SPRINTARS to the size representation

775 scheme and the introduction of aerosol dynamical processes. For consistency

776 between the two versions of the model, assumptions in SPRINTARS-orig are also

777 made in SPRINTARS-bin when possible, but these assumptions may not be

778 optimized to produce the most realistic aerosol size distributions. For example, the

779 size ranges of dust and salt are set between 0.2 to 20 µm, implying that the finer

780 particles are not captured, and the long-range transport of these aerosols may be

781 underestimated. Also, we followed the same emission schemes for salt and dust as

782 in SPRINTARS-orig, but there are many other schemes proposed. Grythe et al.

783 (2014) evaluated 21 different salt source functions and found significant variabilities

784 in sea salt burdens. They also suggested that the dependency on sea surface

785 temperature should be considered, which may explain the unexpected peak of sea

786 salt mass in the Arctic region simulated in both models. For soil dust, several source

787 functions are also proposed based on measurements as well as experimental

788 studies, and the sensitivities to the source functions should also be investigated.

789 5.2 Aerosol mixing state

790   In both SPRINTARS-orig and SPRINTARS-bin, the major aerosol types are

791 represented as external mixtures, which involve simulating particles as consisting of

792 one particular type of aerosol. In the ambient atmosphere, however, aerosols usually

793 exist as internal mixtures of different chemical compositions, for example, from the

794 condensation of sulfuric acid and organics. In order to focus on the effect of size

795 representations, and for a fair comparison with the existing non-microphysical

796 scheme, we did not introduce new internal mixture components to SPRINTARS-bin

797 in this study. We note that the skill score compared to the observations is likely

798 affected by the externally mixed simplification.

799   In particular, the simulated sulfate aerosol sizes may deviate from the observed

800 size distributions due to the mixed-type coagulation and other growth processes that

801 are not implemented in the model. Limited by the external mixture assumption, the

802 coagulation between particles of different aerosol types is not considered.

803 Scavenging by larger particles is an important sink of the finest sulfate particles, and

804 the absence of this effect in these simulations affects the particle number

805 concentrations predicted by NICAM-SPRINTARS-bin. Coagulation with larger sulfate

806 particles is, however, resolved in the simulations here and found to contribute to

807 more than 50% of the total global sink of sulfate particles with diameters smaller than

808 10 nm, and more than 30% for those with diameters between 10 and 30 nm. The

809 coagulation of sulfate with other aerosol types would lead to faster removal of fine

810 particles and the formation of larger particles of higher extinction efficiencies.

811 Besides, the growth processes of sulfate involving other chemical components are

812 not considered in the current model. For example, SOA may condense on the

813 existing sulfate particles, forming larger particles. These missing processes may

814 explain the relatively low AOD values found in industrial regions, where both sulfate

815 and carbonaceous aerosols dominate. The simplified mixing state will likely have led

816 to an overpredicted atmospheric lifetime of fine sulfate particles, resulting in a high

817 number concentrations and Angstrom Exponent at locations distant from the sources.

818 This may explain the overestimated total number concentrations predicted at certain

819 GAW stations (e.g., Bondville and Pallas, Figure 10), as well as the high Angstrom

820 Exponent, predicted in the high-latitude region (Figure 7).

821 Another potential source of error from the externally mixed approach is in the BC

822 mixing state, which is always 100% black carbon (pure soot) in the current model.

823 Freshly emitted BC particles mostly contain elemental carbon, so they are

824 hydrophobic. In reality, emitted BC particles are gradually coated with other non-BC

825 species, including sulfate and SOA, through coagulation and condensation, as well

826 as photochemical oxidation processes. The internal mixing with non-BC material

827 increases the absorption efficiencies (lensing effect) as well as the hygroscopicities.

828 Bond *et al.* (2006) suggested that the absorption of aged aerosols is 50% higher

829 than fresh aerosols, although their results also suggested that the estimate of

830 absorption enhancement also depends on the assumed mixing rules and geometries.

831 Since the mixing of BC with sulfate and OC is not considered in the current model,

832 the absorption enhancement due to BC aging is not captured, and the AOD

833 contributed by BC is likely to be underestimated when the BC particles are far from

834 the source regions. Thus, the BC mixing state should be considered a priority to

835 include in the onward development of SPRINTARS-bin.

836 5.3 Model resolution

837 An advantage of the microphysical model being developed in NICAM-

838 SPRINTARS, is that the model can be seamlessly run for a wide range of different

839 grid resolutions. However, minimizing model-observation discrepancies is not the

840 purpose of this study, so we used the relatively coarse grid resolution for climate

841 simulations and have demonstrated that NICAM-SPRINTARS-bin can still produce

842 reasonable results over the globe at this resolution. It is expected that the low

843 resolution of the grid limits the accuracies in reproducing the observations because

844 the meteorological fields only represent the mean state of regions of hundreds of

845 square kilometers the local terrains are not well resolved. Consequently, the aerosol

846 transport may not reflect the actual transport at measurement stations. In addition,

847 errors are introduced when the emission inventories are mapped on a coarser grid,

848 including the emission strengths and locations. These effects tend to dilute the

849 chemistry and aerosol processes, affecting the spatial distributions of aerosols and

850 also the size distributions of sulfate particles. For example, larger particles are likely

851 to be produced under higher gaseous sulfate concentrations (due to stronger growth).

852 In the cloud-resolving experiments of NICAM-SPRINTARS, cloud processes can

853 be explicitly simulated without the use of cumulus parameterizations. The more

854 realistic simulation of cloud structure and precipitation without changing the source

855　code makes NICAM-SPRINTARS suitable for the investigation of aerosol-cloud

856　interactions over multiple scales. The influence of aerosol concentrations and size

857　distributions on cloud systems has been recognized (e.g., Tao *et al.*, 2007; Ekman *et*

858　*al.*, 2011). It is also suggested that the size representations affect the accuracy in

859　modeling aerosol-cloud interactions (Zhang et al., 2002). However, size-resolving

860　aerosol schemes have been rarely used in cloud-resolving simulations (e.g., Ekman

861　et al., 2006). It is expected that high-resolution experiments using NICAM-

862　SPRINTARS-bin introduced here provide new opportunities to understand aerosol-

863　cloud interactions from a global perspective.

864　5.4 Aerosol-cloud interactions

865　　To investigate the potential impact on aerosol-cloud interactions by the size-

866　resolving model, we calculate the activation diameters (minimum diameter of

867　aerosols to be activated) of different aerosol types using the schemes proposed in

868　Abdul-Razzak and Ghan (2000, 2002). The scheme has been proposed for the use

869　of multiple aerosol populations represented by size bins and considers the

870　supersaturation, updraft velocities, aerosol hygroscopicity as well as the size

871　distributions of all aerosols simulated in the model. These online-calculated

872　activation diameters are not used in calculating in-cloud scavenging and cloud

873　activation processes (Section 3.5a), and thus should be regarded as an initial

874　investigation of size dependencies and variabilities of the CCN properties in global

875　model simulations.

876　　As shown in Fig. 13, the activation diameters are highly variable, which is not

877　likely to be captured by SPRINTARS-orig. At low altitudes, the activation diameters

878　are mainly within the smallest size bins, and the whole aerosol populations are likely

879 to be activated. The activation diameters tend to increase with increasing altitude for

880 the activation diameters of sulfate and OC, for instance, mostly above 200 nm at 7

881 km (Figs 13c and 13d). Thus, it is expected that SPRINTARS-bin can better capture

882 the effect of aerosols on cloud microphysics when used in high-resolution

883 simulations. It should be noted that the activation diameters calculated here are only

884 an estimation because the updraft velocities are not well resolved in this low-

885 resolution experiment. By combining the size distributions and the resolved updraft

886 velocities provided by the cloud-resolving NICAM model, the number concentrations

887 of CCN being activated can be better estimated. The more accurate calculation of

888 CCN activation also affects the size distributions of aerosols due to in-cloud

889 scavenging and recycling processes (Ekman *et al.*, 2011). Such consideration of

890 recycling of aerosols from cloud evaporation is possible only when a detailed cloud

891 microphysics scheme is used.

892

893 **6 Summary**

894 We implemented a full sectional microphysics scheme (SPRINTARS-bin) into the

895 aerosol model SPRINTARS and evaluated its predictions within climate-resolution

896 simulations in the global model NICAM. To investigate the fundamental differences

897 in the model behaviors, assumptions in the original SPRINTARS model

898 (SPRINTARS-orig) are followed when possible. As the same emission inventories or

899 emission schemes are used, and the wind fields are nudged to a meteorological re-

900 analysis, the overall aerosol burden does not differ substantially between the two

901 models, resulting in similar distributions of surface mass concentrations and aerosol

902 optical depth.

In SPRINTARS-orig, size distributions of soil dust and sea salt are represented by 10 and 4 size bins, respectively, whereas 20 bins are used to resolve the size distribution of each aerosol component in SPRINTARS-bin. Therefore, different behaviors between the two models are principally attributed to the size distribution resolution of these two types of coarse particles. For carbonaceous aerosols, the initial size distribution in SPRINTARS-bin is assumed to be the same as the prescribed log-normal distribution in SPRINTARS-orig, so that the differences are mostly due to size-dependencies of the deposition processes. The overall picture for these three aerosol types is not greatly changed, although NICAM-SPRINTARS-bin predicts vertical transport to slightly higher levels. In the microphysical approach of SPRINTARS-bin, the size distribution of sulfate is entirely determined from aerosol microphysical processes (e.g., nucleation, coagulation, and condensation). As a result, the two models demonstrate different sulfate transport within NICAM due to the different size representations of sulfate particles. Particularly, NICAM-SPRINTARS-bin simulated a stronger transport of finest particles to regions remote from sources of pollution.

The largest differences between the two models are seen in the more size-relevant quantities: number concentrations and Angstrom Exponent (AE). The number concentrations are highly sensitive to the presence of ultra-fine aerosol particles. As NICAM-SPRINTARS-orig does not resolve the size distributions of sulfate and carbonaceous aerosols, the number concentrations at GAW and EUSAAR stations are strongly underestimated. By contrast, NICAM-SPRINTARS-bin resolves new particle formation and coagulation and predicts much higher number concentrations as the finest particles are resolved. These fine particles are transported to the Arctic and Antarctica. Comparison with observations demonstrates

928 that NICAM-SPRINTARS-bin improves the estimation of total number concentrations

929 at GAW stations, number concentrations of fine particles at EUSAAR stations, as

930 well as the AE values closer to the observations in AERONET. However, the

931 performance in predicting the number concentrations of coarse particles, which have

932 a higher potential to act as CCN in warm clouds, is not greatly improved.

933 Although the simulations are run at a climate-scale resolution and with model

934 parameters that have not yet been optimized, the results are generally in good

935 agreement with different observations. The model-observation differences highlight

936 the need for sensitivity experiments to test different schemes and parameter settings

937 within uncertainties to seek more realistic simulations of aerosol size distributions.

938 The evaluation suggests that internally-mixed aerosol components and BC aging

939 should also be included. SPRINTARS-bin provides a framework to incorporate

940 improved size-dependent representations of aerosol processes, including more

941 sophisticated emission mechanisms and source functions, cloud activation schemes,

942 and aerosol nucleation schemes. The size information is also expected to improve

943 our knowledge in understanding and quantifying the interactions of aerosols with

944 radiation and clouds.

945 **Supplement**

946 Supplementary Table S1 shows the computation time ratios and total AOD root-

947 mean-square deviation for a set of 1-week long simulations using NICAM-

948 SPRINTARS-orig and NICAM-SPRINTARS-bin with different numbers of bins.

949 Supplementary Tables S2 and S3 shows the growth factor parameters and refractive

950 indices used in the simulations, respectively.

951

967

References

968

969 Abdul-Razzak, H., and S. J. Ghan, 2000: A parameterization of aerosol activation: 2.

970   Multiple aerosol types. *J. Geophys. Res.*, **105D**, 6837–6844.

971 Abdul-Razzak, H., and S. J. Ghan, 2002: A parameterization of aerosol activation 3.

972   Sectional representation. *J. Geophys. Res.*, **107D**, AAC 1-1–AAC 1-6.

973 Abdul-Razzak, H., S. J. Ghan, and C. Rivera-Carpio, 1998: A parameterization of

974   aerosol activation: 1. Single aerosol type. *J. Geophys. Res.*, **103D**, 6123–6131.

975 Adams, P. J., and J. H. Seinfeld, 2002: Predicting global aerosol size distributions in

976   general circulation models. *J. Geophys. Res.*, **107D**, AAC 4-1–AAC 4-23.

977 Alfaro, S. C., and L. Gomes, 2001: Modeling mineral aerosol production by wind

978   erosion: Emission intensities and aerosol size distributions in source areas. *J.*

979   *Geophys. Res.*, **106D**, 18075–18084.

980 Andreae, M. O., and D. Rosenfeld, 2008: Aerosol–cloud–precipitation interactions.

981   Part 1. The nature and sources of cloud-active aerosols. *Earth-Sci. Rev.*, **89**,

982   13–41.

983 Anttila, T., V.-M. Kerminen, and K. E. J. Lehtinen, 2010: Parameterizing the

984   formation rate of new particles: The effect of nuclei self-coagulation. *J. Aerosol*

985   *Sci.*, **41**, 621–636.

986 Asmi, A., A. Wiedensohler, P. Laj, A.-M. Fjaeraa, K. Sellegri, W. Birmili, E.

987   Weingartner, U. Baltensperger, V. Zdimal, N. Zikova, J.-P. Putaud, A. Marinoni,

988   P. Tunved, H.-C. Hansson, M. Fiebig, N. Kivekäs, H. Lihavainen, E. Asmi, V.

989   Ulevicius, P. P. Aalto, E. Swietlicki, A. Kristensson, N. Mihalopoulos, N. Kalivitis,

990   I. Kalapov, G. Kiss, G. de Leeuw, B. Henzing, R. M. Harrison, D. Beddows, C.

991   O'Dowd, S. G. Jennings, H. Flentje, K. Weinhold, F. Meinhardt, L. Ries, and M.

992   Kulmala, 2011: Number size distributions and seasonality of submicron particles

993   in Europe 2008–2009. *Atmos. Chem. Phys.*, **11**, 5505–5538.

994 Bates, T. S., R. J. Charlson, and R. H. Gammon, 1987: Evidence for the climatic role

995   of marine biogenic sulphur. *Nature,* **329**, 319–321.

996 Bergman, T., V.-M. Kerminen, H. Korhonen, K. J. Lehtinen, R. Makkonen, A. Arola, T.

997   Mielonen, S. Romakkaniemi, M. Kulmala, and H. Kokkola, 2012: Evaluation of

998   the sectional aerosol microphysics module SALSA implementation in ECHAM5-

999   HAM aerosol-climate model. *Geosci. Model Dev.*, **5**, 845–868.

1000 Bond, T. C., G. Habib, and R. W. Bergstrom, 2006: Limitations in the enhancement

1001   of visible light absorption due to mixing state. *J. Geophys. Res.*, **111**, D20211,

1002   doi:10.1029/2006JD007315.

1003 Boucher, O., D. Randall, P. Artaxo, C. S. Bretherton, G. Feingold, P. Forster, V.-M.

1004   Kerminen, Y. Kondo, H. Liao, U. Lohmann, P. Rasch, S. K. Satheesh, S.

1005   Sherwood, B. Stevens, X.-Y. Zhang, 2013: Clouds and aerosols. *Climate*

1006   *Change 2013: The Physical Science Basis. Contribution of Working Group I to*

1007   *the Fifth Assessment Report of the Intergovernmental Panel on Climate Change*.

1008 Stocker, T.F., D. Qin, G.-K. Plattner, M. M. B. Tignor, S. K. Allen, J. Boschung, A.

1009   Nauels, Y. Xia, V. Bex, and P. M. Midgley (eds.), Cambridge University Press,

1010   571–658.

1011 Ching, J., R. A. Zaveri, R. C. Easter, N. Riemer, and J. D. Fast, 2016: A three-

1012   dimensional sectional representation of aerosol mixing state for simulating

optical properties and cloud condensation nuclei. *J. Geophys. Res.: Atmos.*, **121**, 5912–5929.

d'Almeida, G. A., and L. Schütz, 1983: Number, mass and volume distributions of mineral aerosol and soils of the Sahara. *J. Appl. Meteor. Climatol.*, **22**, 233–243.

d'Almeida, G. A., P. Koepke, and E. P. Shettle, 1991: *Atmospheric Aerosols: Global Climatology and Radiative Characteristics*. A Deepak Pub. 561 pp.

Dai, T., D. Goto, N. A. J. Schutgens, X. Dong, G. Shi, and T. Nakajima, 2014: Simulated aerosol key optical properties over global scale using an aerosol transport model coupled with a new type of dynamic core. *Atmos. Environ.*, **82**, 71–82.

Dai, T., Y. Cheng, P. Zhang, G. Shi, M. Sekiguchi, K. Suzuki, D. Goto, and T. Nakajima, 2018: Impacts of meteorological nudging on the global dust cycle simulated by NICAM coupled with an aerosol model. *Atmos. Environ.*, **190**, 99–115.

Diehl, T., A. Heil, M. Chin, X. Pan, D. Streets, M. Schultz, and S. Kinne, 2012: Anthropogenic, biomass burning, and volcanic emissions of black carbon, organic carbon, and SO_2 from 1980 to 2010 for hindcast model experiments. *Atmos. Chem. Phys. Discuss.*, **12**, 24895–24954.

van der Does, M., L. F. Korte, C. I. Munday, G.-J. A. Brummer, and J.-B. W. Stuut, 2016: Particle size traces modern Saharan dust transport and deposition across the equatorial North Atlantic. *Atmos. Chem. Phys.*, **16**, 13697–13710.

Ekman, A. M. L., C. Wang, J. Ström, and R. Krejci, 2006: Explicit simulation of aerosol physics in a cloud-resolving model: Aerosol transport and processing in

1036   the free troposphere. *J. Atmos. Sci.*, **63**, 682–696.

1037   Ekman, A. M. L., A. Engström, and A. Söderberg, 2011: Impact of two-way aerosol-

1038   cloud interaction and changes in aerosol size distribution on simulated aerosol-

1039   induced deep convective cloud sensitivity. *J. Atmos. Sci.*, **68**, 685–698.

1040   Fan, J., Y. Wang, D. Rosenfeld, and X. Liu, 2016: Review of aerosol–cloud

1041   interactions: Mechanisms, significance, and challenges. *J. Atmos. Sci.*, **73**,

1042   4221–4252.

1043   Foret, G., G. Bergametti, F. Dulac, and L. Menut, 2006: An optimized particle size

1044   bin scheme for modeling mineral dust aerosol. *J. Geophys. Res.*, **111**, D17310,

1045   doi:10.1029/2005JD006797.

1046   Gong, S. L., 2003: A parameterization of sea-salt aerosol source function for sub-

1047   and super-micron particles. *Global Biogeochem. Cycles*, **17**, 1097,

1048   doi:10.1029/2003GB002079.

1049   Gong, S. L., and L. A. Barrie, 2003: Simulating the impact of sea salt on global nss

1050   sulphate aerosols. *J. Geophys. Res.*, **108D**, 4516, doi:10.1029/2002JD003181.

1051   Gong, S. L., L. A. Barrie, J.-P. Blanchet, K. von Salzen, U. Lohmann, G. Lesins, L.

1052   Spacek, L. M. Zhang, E. Girard, H. Lin, R. Leaitch, H. Leighton, P. Chylek, and

1053   P. Huang, 2003: Canadian Aerosol Module: A size-segregated simulation of

1054   atmospheric aerosol processes for climate and air quality models 1. Module

1055   development. *J. Geophys. Res.*, **108D**, AAC 3-1–AAC 3-16.

1056   Goto, D., T. Nakajima, T. Takemura, and K. Sudo, 2011: A study of uncertainties in

1057   the sulfate distribution and its radiative forcing associated with sulfur chemistry

1058   in a global aerosol model. *Atmos. Chem. Phys.*, **11**, 10889–10910.

1059 Goto, D., T. Dai, M. Satoh, H. Tomita, J. Uchida, S. Misawa, T. Inoue, H. Tsuruta, K.

1060   Ueda, C. F. S. Ng, A. Takami, N. Sugimoto, A. Shimizu, T. Ohara, and T.

1061   Nakajima, 2015: Application of a global nonhydrostatic model with a stretched-

1062   grid system to regional aerosol simulations around Japan. *Geosci. Model Dev.*,

1063   **8**, 235–259.

1064 Goto, D., T. Nakajima, D. Tie, H. Yashiro, Y. Sato, K. Suzuki, J. Uchida, S. Misawa,

1065   R. Yonemoto, T. T. N. Trieu, H. Tomita, and M. Satoh, 2018: Multi-scale

1066   simulations of atmospheric pollutants using a non-hydrostatic icosahedral

1067   atmospheric model. *Land-Atmospheric Research Applications in South and*

1068   *Southeast Asia*. Vadrevu, K., T. Ohara, and C. Justice (eds.), Springer, Cham.

1069   277–302.

1070 Goto, D., M. Kikuchi, K. Suzuki, M. Hayasaki, M. Yoshida, T. M. Nagao, M. Choi, J.

1071   Kim, N. Sugimoto, A. Shimizu, E. Oikawa, and T. Nakajima, 2019: Aerosol

1072   model evaluation using two geostationary satellites over East Asia in May 2016.

1073   *Atmos. Res.*, **217**, 93–113.

1074 Goto, D., Y. Sato, H. Yashiro, K. Suzuki, E. Oikawa, R. Kudo, T. M. Nagao, and T.

1075   Nakajima, 2020: Global aerosol simulations using NICAM.16 on a 14 km grid

1076   spacing for a climate study: Improved and remaining issues relative to a lower-

1077   resolution model. *Geosci. Model Dev.*, **13**, 3731–3768.

1078 Grythe, H., J. Ström, R. Krejci, P. Quinn, and A. Stohl, 2014: A review of sea-spray

1079   aerosol source functions using a large global set of sea salt aerosol

1080   concentration measurements. *Atmos. Chem. Phys.*, **14**, 1277–1297.

1081 Haywood, J., and O. Boucher, 2000: Estimates of the direct and indirect radiative

forcing due to tropospheric aerosols: A review. *Rev. Geophys.*, **38**, 513–543.

Holben, B. N., T. F. Eck, I. Slutsker, D. Tanré, J. P. Buis, A. Setzer, E. Vermote, J. A. Reagan, Y. J. Kaufman, T. Nakajima, F. Lavenu, I. Jankowiak, and A. Smirnov, 1998: AERONET —A federated instrument network and data archive for aerosol characterization. *Remote Sens. Environ.*, **66**, 1–16.

Jacobson, M. Z., 1997a: Development and application of a new air pollution modeling system—II. Aerosol module structure and design. *Atmos. Environ.*, **31**, 131–144.

Jacobson, M. Z., 1997b: Numerical techniques to solve condensational and dissolutional growth equations when growth is coupled to reversible reactions. *Aerosol Sci. Technol.*, **27**, 491–498.

Jacobson, M. Z., 2005: Coagulation. *Fundamentals of Atmospheric Modeling*. Cambridge University Press, 494–524.

Jacobson, M. Z., R. P. Turco, E. J. Jensen, and O. B. Toon, 1994: Modeling coagulation among particles of different composition and size. *Atmos. Environ.*, **28**, 1327–1338.

Janssens-Maenhout, G., M. Crippa, D. Guizzardi, F. Dentener, M. Muntean, G. Pouliot, T. Keating, Q. Zhang, J. Kurokawa, R. Wankmüller, H. Denier van der Gon, J. J. P. Kuenen, Z. Klimont, G. Frost, S. Darras, B. Koffi, and M. Li, 2015: HTAP_v2.2: A mosaic of regional and global emission grid maps for 2008 and 2010 to study hemispheric transport of air pollution. *Atmos. Chem. Phys.*, **15**, 11411–11432.

Kerminen, V.-M., and M. Kulmala, 2002: Analytical formulae connecting the "real"

and the "apparent" nucleation rate and the nuclei number concentration for atmospheric nucleation events. *J. Aerosol Sci.*, **33**, 609–622.

Kodama, C., Y. Yamada, A. T. Noda, K. Kikuchi, Y. Kajikawa, T. Nasuno, T. Tomita, T. Yamaura, H. G. Takahashi, M. Hara, Y. Kawatani, M. Satoh, and M. Sugi, 2015: A 20-year climatology of a NICAM AMIP-type simulation. *J. Meteor. Soc. Japan*, **93**, 393–424.

Kok, J. F., 2011a: A scaling theory for the size distribution of emitted dust aerosols suggests climate models underestimate the size of the global dust cycle. *Proc. Natl. Acad. Sci. U. S. A.*, **108**, 1016–1021.

Kok, J. F., 2011b: Does the size distribution of mineral dust aerosols depend on the wind speed at emission? *Atmos. Chem. Phys.*, **11**, 10149–10156.

Kokkola, H., H. Korhonen, K. E. J. Lehtinen, R. Makkonen, A. Asmi, S. Järvenoja, T. Anttila, A.-I. Partanen, M. Kulmala, H. Järvinen, A. Laaksonen, and V.-M. Kerminen, 2008: SALSA - a sectional aerosol module for large scale applications. *Atmos. Chem. Phys.*, **8**, 2469–2483.

Kokkola, H., T. Kühn, A. Laakso, T. Bergman, K. E. J. Lehtinen, T. Mielonen, A. Arola, S. Stadtler, H. Korhonen, S. Ferrachat, U. Lohmann, D. Neubauer, I. Tegen, C. S.-L. Drian, M. G. Schultz, I. Bey, P. Stier, N. Daskalakis, C. L. Heald, and S. Romakkaniemi, 2018: SALSA2.0: The sectional aerosol module of the aerosol–chemistry–climate model ECHAM6.3.0-HAM2.3-MOZ1.0. *Geosci. Model Dev.*, **11**, 3833–3863.

Kulmala, M., A. Laaksonen, and L. Pirjola, 1998: Parameterizations for sulfuric acid/water nucleation rates. *J. Geophys. Res.*, **103D**, 8301–8307.

1128 Kulmala, M., K. E. J. Lehtinen, and A. Laaksonen, 2006: Cluster activation theory as

1129   an explanation of the linear dependence between formation rate of 3 nm

1130   particles and sulphuric acid concentration. *Atmos. Chem. Phys.*, **6**, 787–793.

1131 Lee, Y. H., and P. J. Adams, 2012: A fast and efficient version of the TwO-Moment

1132   Aerosol Sectional (TOMAS) global aerosol microphysics model. *Aerosol Sci.*

1133   *Technol.*, **46**, 678–689.

1134 Lehtinen, K. E. J., M. Dal Maso, M. Kulmala, and V.-M. Kerminen, 2007: Estimating

1135   nucleation rates from apparent particle formation rates and vice versa: Revised

1136   formulation of the Kerminen–Kulmala equation. *J. Aerosol Sci.*, **38**, 988–994.

1137 Lohmann, U., and J. Feichter, 2005: Global indirect aerosol effects: A review. *Atmos.*

1138   *Chem. Phys.*, **5**, 715–737.

1139 Luo, Y., X. Zheng, T. Zhao, and J. Chen, 2014: A climatology of aerosol optical

1140   depth over China from recent 10 years of MODIS remote sensing data. *Int. J.*

1141   *Climatol.*, **34**, 863–870.

1142 Määttänen A., J. Merikanto, H. Henschel, J. Duplissy, R. Makkonen, I. K. Ortega,

1143   and H. Vehkamäki, 2018: New parameterizations for neutral and ion-induced

1144   sulfuric acid-water particle formation in nucleation and kinetic regimes. *J.*

1145   *Geophys. Res.: Atmos.*, **123**, 1269–1296.

1146 Mann, G. W., K. S. Carslaw, D. V. Spracklen, D. A. Ridley, P. T. Manktelow, M. P.

1147   Chipperfield, S. J. Pickering, and C. E. Johnson, 2010: Description and

1148   evaluation of GLOMAP-mode: A modal global aerosol microphysics model for

1149   the UKCA composition-climate model. *Geosci. Model Dev.*, **3**, 519–551.

1150 Mann, G. W., K. S. Carslaw, D. A. Ridley, D. V. Spracklen, K. J. Pringle, J. Merikanto,

H. Korhonen, J. P. Schwarz, L. A. Lee, P. T. Manktelow, M. T. Woodhouse, A. Schmidt, T. J. Breider, K. M. Emmerson, C. L. Reddington, M. P. Chipperfield, and S. J. Pickering, 2012: Intercomparison of modal and sectional aerosol microphysics representations within the same 3-D global chemical transport model. *Atmos. Chem. Phys.*, **12**, 4449–4476.

Mann, G. W., K. S. Carslaw, C. L. Reddington, K. J. Pringle, M. Schulz, A. Asmi, D. V. Spracklen, D. A. Ridley, M. T. Woodhouse, L. A. Lee, K. Zhang, S. J. Ghan, R. C. Easter, X. Liu, P. Stier, Y. H. Lee, P. J. Adams, H. Tost, J. Lelieveld, S. E. Bauer, K. Tsigaridis, T. P. C. van Noije, A. Strunk, E. Vignati, N. Bellouin, M. Dalvi, C. E. Johnson, T. Bergman, H. Kokkola, K. von Salzen, F. Yu, G. Luo, A. Petzold, J. Heintzenberg, A. Clarke, J. A. Ogren, J. Gras, U. Baltensperger, U. Kaminski, S. G. Jennings, C. D. O'Dowd, R. M. Harrison, D. C. S. Beddows, M. Kulmala, Y. Viisanen, V. Ulevicius, N. Mihalopoulos, V. Zdimal, M. Fiebig, H.-C. Hansson, E. Swietlicki, and J. S. Henzing, 2014: Intercomparison and evaluation of global aerosol microphysical properties among AeroCom models of a range of complexity. *Atmos. Chem. Phys*, **14**, 4679–4713.

Maring, H., D. L. Savoie, M. A. Izaguirre, L. Custals, and J. S. Reid, 2003: Mineral dust aerosol size distribution change during atmospheric transport. *J. Geophys. Res.*, **108D**, 8592, doi:10.1029/2002JD002536.

Marti, J. J., A. Jefferson, X. P. Cai, C. Richert, P. H. McMurry, and F. Eisele, 1997: H_2SO_4 vapor pressure of sulfuric acid and ammonium sulfate solutions. *J. Geophys. Res.*, **102D**, 3725–3735.

Matsui, H., 2017: Development of a global aerosol model using a two-dimensional sectional method: 1. Model design. *J. Adv. Model. Earth Syst.*, **9**, 1921–1947.

1175   Matsui, H., and N. Mahowald, 2017: Development of a global aerosol model using a

1176   two-dimensional sectional method: 2. Evaluation and sensitivity simulations. *J.*

1177   *Adv. Model. Earth Syst.*, **9**, 1887–1920.

1178   Matsui, H., M. Koike, Y. Kondo, J. D. Fast, and M. Takigawa, 2014: Development of

1179   an aerosol microphysical module: Aerosol Two-dimensional bin module for

1180   foRmation and Aging Simulation (ATRAS). *Atmos. Chem. Phys.*, **14**, 10315–

1181   10331.

1182   Miura, H., M. Satoh, T. Nasuno, A. T. Noda, and K. Oouchi, 2007: A Madden-Julian

1183   Oscillation event realistically simulated by a global cloud-resolving model.

1184   *Science*, **318**, 1763–1765.

1185   Miyamoto, Y., Y. Kajikawa, R. Yoshida, T. Yamaura, H. Yashiro, and H. Tomita,

1186   2013: Deep moist atmospheric convection in a subkilometer global simulation.

1187   *Geophys. Res. Lett.*, **40**, 4922–4926.

1188   Monahan, E. C., D. E. Spiel, and K. L. Davidson, 1986: A model of marine aerosol

1189   generation via whitecaps and wave disruption. *Oceanic Whitecaps: And Their*

1190   *Role in Air-Sea Exchange Processes*. Monahan, E. C., and G. M. Niocaill (eds.),

1191   Springer, Dordrecht, 167–174.

1192   NOAA/NCEP, 2000: NCEP FNL Operational Model Global Tropospheric Analyses,

1193   continuing from July 1999. *Res. Data Arch. Natl. Cent. Atmos. Res. Comput. Inf.*

1194   *Syst. Lab.*, https://doi.org/10.5065/D6M043C6. (Accessed 01 Feb 2020).

1195   Park, S. S., T. Takemura, and S.-W. Kim, 2018: Comparison of aerosol optical depth

1196   between observation and simulation from MIROC-SPRINTARS: Effects of

1197   temporal inhomogeneous sampling. *Atmos. Environ.*, **186**, 56–73.

1198   Philippin, S., P. Laj, J.-P. Putaud, A. Wiedensohler, G. De Leeuw, A. M. Fjaeraa, U.

1199   Platt, U. Baltensperger, and M. Fiebig, 2009: EUSAAR - An unprecedented

1200   network of aerosol observation in Europe. *Earozoru Kenkyu*, **24**, 78–83.

1201   Platnick, S., M. D. King, K. G. Meyer, G. Wind, N. Amarasinghe, B. Marchant, G. T.

1202   Arnold, Z. Zhang, P. A. Hubanks, B. Ridgway, and J. Riedi, 2015: MODIS

1203   atmosphere L3 monthly product. *NASA MODIS Adapt. Process. Syst. Goddard*

1204   *Sp. Flight Center, USA*, http://dx.doi.org/10.5067/MODIS/MOD08_M3.006.

1205   Sato, Y., D. Goto, T. Michibata, K. Suzuki, T. Takemura, H. Tomita, and T. Nakajima,

1206   2018: Aerosol effects on cloud water amounts were successfully simulated by a

1207   global cloud-system resolving model. *Nat. Commun.*, **9**, 985,

1208   doi:10.1038/s41467-018-03379-6.

1209   Satoh, M., T. Matsuno, H. Tomita, H. Miura, T. Nasuno, and S. Iga, 2008:

1210   Nonhydrostatic icosahedral atmospheric model (NICAM) for global cloud

1211   resolving simulations. *J. Comput. Phys.*, **227**, 3486–3514.

1212   Satoh, M., H. Tomita, H. Yashiro, H. Miura, C. Kodama, T. Seiki, A. T. Noda, Y.

1213   Yamada, D. Goto, M. Sawada, T. Miyoshi, Y. Niwa, M. Hara, T. Ohno, S. Iga, T.

1214   Arakawa, T. Inoue, and H. Kubokawa, 2014: The non-hydrostatic icosahedral

1215   atmospheric model: Description and development. *Prog. Earth Planet. Sci.*, **1**,

1216   18, doi:10.1186/s40645-014-0018-1.

1217   Satoh, M., B. Stevens, F. Judt, M. Khairoutdinov, S.-J. Lin, W. M. Putman, and P.

1218   Düben, 2019: Global cloud-resolving models. *Curr. Climate Change Rep.*, **5**,

1219   172–184.

1220   Schulz, M., Y. J. Balkanski, W. Guelle, and F. Dulac, 1998: Role of aerosol size

distribution and source location in a three-dimensional simulation of a Saharan dust episode tested against satellite-derived optical thickness. *J. Geophys. Res.*, **103D**, 10579–10592.

Spracklen, D. V., K. J. Pringle, K. S. Carslaw, M. P. Chipperfield, and G. W. Mann, 2005: A global off-line model of size-resolved aerosol microphysics: I. Model development and prediction of aerosol properties. *Atmos. Chem. Phys.*, **5**, 2227–2252.

Stevens, B., and S. Bony, 2013: What are climate models missing? *Science*, **340**, 1053–1054.

Sudo, K., M. Takahashi, J. Kurokawa, and H. Akimoto, 2002: CHASER: A global chemical model of the troposphere 1. Model description. *J. Geophys. Res.*, **107D**, ACH 7-1–ACH 7-20.

Suzuki, K., T. Nakajima, M. Satoh, H. Tomita, T. Takemura, T. Y. Nakajima, and G. L. Stephens, 2008: Global cloud-system-resolving simulation of aerosol effect on warm clouds. *Geophys. Res. Lett.*, **35**, L19817, doi:10.1029/2008GL035449.

Takemura, T., H. Okamoto, Y. Maruyama, A. Numaguti, A. Higurashi, and T. Nakajima, 2000: Global three-dimensional simulation of aerosol optical thickness distribution of various origins. *J. Geophys. Res.*, **105D**, 17853–17873.

Takemura, T., T. Nakajima, A. Higurashi, S. Ohta, and N. Sugimoto, 2003: Aerosol distributions and radiative forcing over the Asian Pacific region simulated by Spectral Radiation-Transport Model for Aerosol Species (SPRINTARS). *J. Geophys. Res.*, **108D**, 8659, doi:10.1029/2002JD003210.

Takemura, T., T. Nozawa, S. Emori, T. Y. Nakajima, and T. Nakajima, 2005:

Simulation of climate response to aerosol direct and indirect effects with aerosol transport-radiation model. *J. Geophys. Res.*, **110**, D02202, doi:10.1029/2004JD005029.

Tao, W.-K., X. Li, A. Khain, T. Matsui, S. Lang, and J. Simpson, 2007: Role of atmospheric aerosol concentration on deep convective precipitation: Cloud-resolving model simulations. *J. Geophys. Res.*, **112**, D24S18, doi:10.1029/2007JD008728.

Textor, C., M. Schulz, S. Guibert, S. Kinne, Y. Balkanski, S. Bauer, T. Berntsen, T. Berglen, O. Boucher, M. Chin, F. Dentener, T. Diehl, R. Easter, H. Feichter, D. Fillmore, S. Ghan, P. Ginoux, S. Gong, A. Grini, J. Hendricks, L. Horowitz, P. Huang, I. Isaksen, I. Iversen, S. Kloster, D. Koch, A. Kirkevåg, J. E. Kristjansson, M. Krol, A. Lauer, J. F. Lamarque, X. Liu, V. Montanaro, G. Myhre, J. Penner, G. Pitari, S. Reddy, Ø. Seland, P. Stier, T. Takemura, and X. Tie, 2006: Analysis and quantification of the diversities of aerosol life cycles within AeroCom. *Atmos. Chem. Phys.*, **6**, 1777–1813.

Tomita, H., and M. Satoh, 2004: A new dynamical framework of nonhydrostatic global model using the icosahedral grid. *Fluid Dyn. Res.*, **34**, 357–400.

Tomita, H., H. Miura, S. Iga, T. Nasuno, and M. Satoh, 2005: A global cloud-resolving simulation: Preliminary results from an aqua planet experiment. *Geophys. Res. Lett.*, **32**, L08805, doi:10.1029/2005GL022459.

Uchida, J., M. Mori, H. Nakamura, M. Satoh, K. Suzuki, and T. Nakajima, 2016: Error and energy budget analysis of a nonhydrostatic stretched-grid global atmospheric model. *Mon. Wea. Rev.*, **144**, 1423–1447.

1267 Uchida, J., M. Mori, M. Hara, M. Satoh, D. Goto, T. Kataoka, K. Suzuki, and T.

1268   Nakajima, 2017: Impact of lateral boundary errors on the simulation of clouds

1269   with a nonhydrostatic regional climate model. *Mon. Wea. Rev.*, **145**, 5059–5082.

1270 Vehkamäki, H., M. Kulmala, I. Napari, K. E. J. Lehtinen, C. Timmreck, M. Noppel,

1271   and A. Laaksonen, 2002: An improved parameterization for sulfuric acid–water

1272   nucleation rates for tropospheric and stratospheric conditions. *J. Geophys. Res.*,

1273   **107D**, AAC 3-1–AAC 3-10.

1274 Wei, J., Y. Peng, J. Guo, and L. Sun, 2019: Performance of MODIS Collection 6.1

1275   Level 3 aerosol products in spatial-temporal variations over land. *Atmos.*

1276   *Environ.*, **206**, 30–44.

1277 Weisenstein, D. K., J. E. Penner, M. Herzog, and X. Liu, 2007: Global 2-D

1278   intercomparison of sectional and modal aerosol modules. *Atmos. Chem. Phys.*,

1279   **7**, 2339–2355.

1280 Whitby, K. T., 1978: The physical characteristics of sulfur aerosols. *Atmos. Environ.*,

1281   **12**, 135–159.

1282 Yu, F., and G. Luo, 2009: Simulation of particle size distribution with a global aerosol

1283   model: Contribution of nucleation to aerosol and CCN number concentrations.

1284   *Atmos. Chem. Phys.*, **9**, 7691–7710.

1285 Zhang, Y., R. C. Easter, S. J. Ghan, and H. Abdul-Razzak, 2002: Impact of aerosol

1286   size representation on modeling aerosol-cloud interactions. *J. Geophys. Res.*,

1287   **107D**, AAC 4-1–AAC 4-17.

1288

1310   Fig. 11 Scatter plot of the annual averages of particle number concentrations at

1311   EUSAAR stations

1312   Fig. 12 Scatter plot of annual averages of AOD and Angstrom at AERONET stations

1313   Fig. 13   Histogram of the activation diameters of different aerosol types at certain

1314   heights

1315

1316
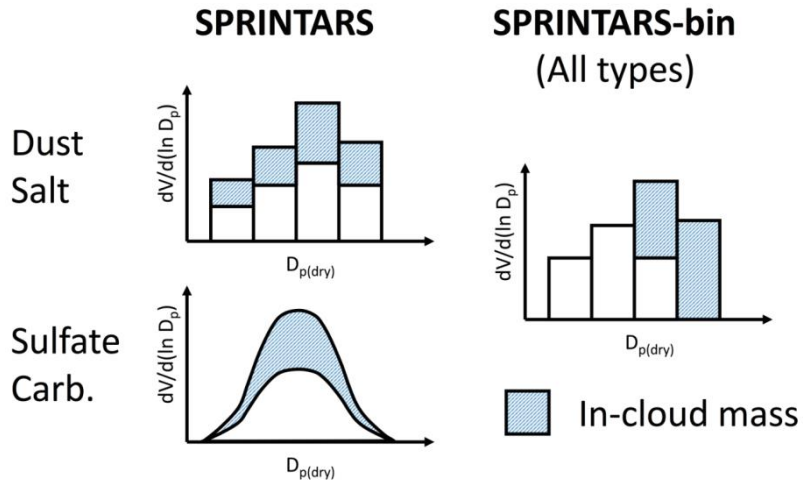
1317

1318 Fig. 1   Representations of in-cloud scavenging scheme in SPRINTARS-orig and

1319 SPRINTARS-bin, given the same in-cloud mass fraction. In SPRINTARS-orig, the in-

1320 cloud mass fractions do not depend on the aerosol sizes. In SPRINTARS-bin, the

1321 largest particles are preferentially assumed to be in-cloud as they are more likely to

1322 become CCNs.

1323

1324

1325

1326

1327
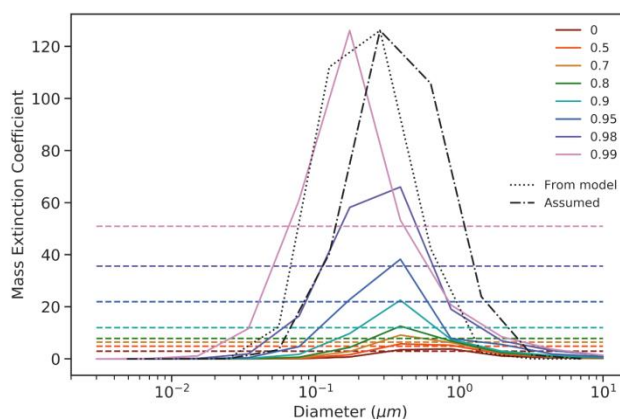
1328

1329   Fig. 2   Mass extinction coefficients of sulfate, as used in SPRINTARS-orig (dashed

1330   line) and SPRINTARS-bin (solid line). Different colors represent the values at

1331   different relative humidity. Black lines indicate the particle size distributions. In

1332   SPRINTARS-orig, a bulk mass extinction coefficient is calculated based on the

1333   assumed size distribution (dash-dot line), whereas in SPRINTARS-bin, each size bin

1334   exhibits different mass extinction coefficients, so the optical properties can be

1335   captured when the size distribution differs from the assumed one (e.g., dotted line).

1336
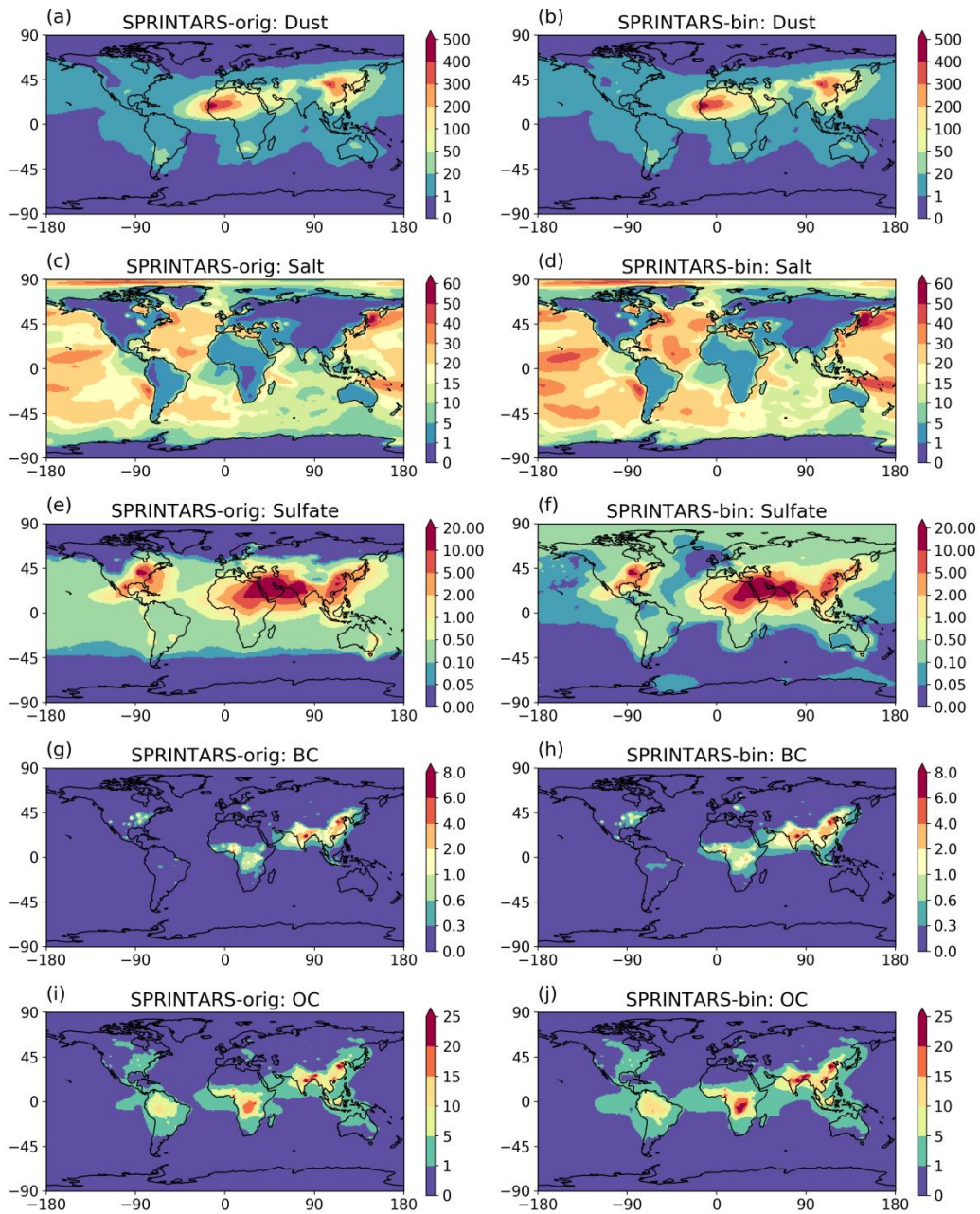
Fig. 3 Spatial distributions of the annually-averaged surface mass concentrations (μg m^{-3}) of each aerosol type.

1341
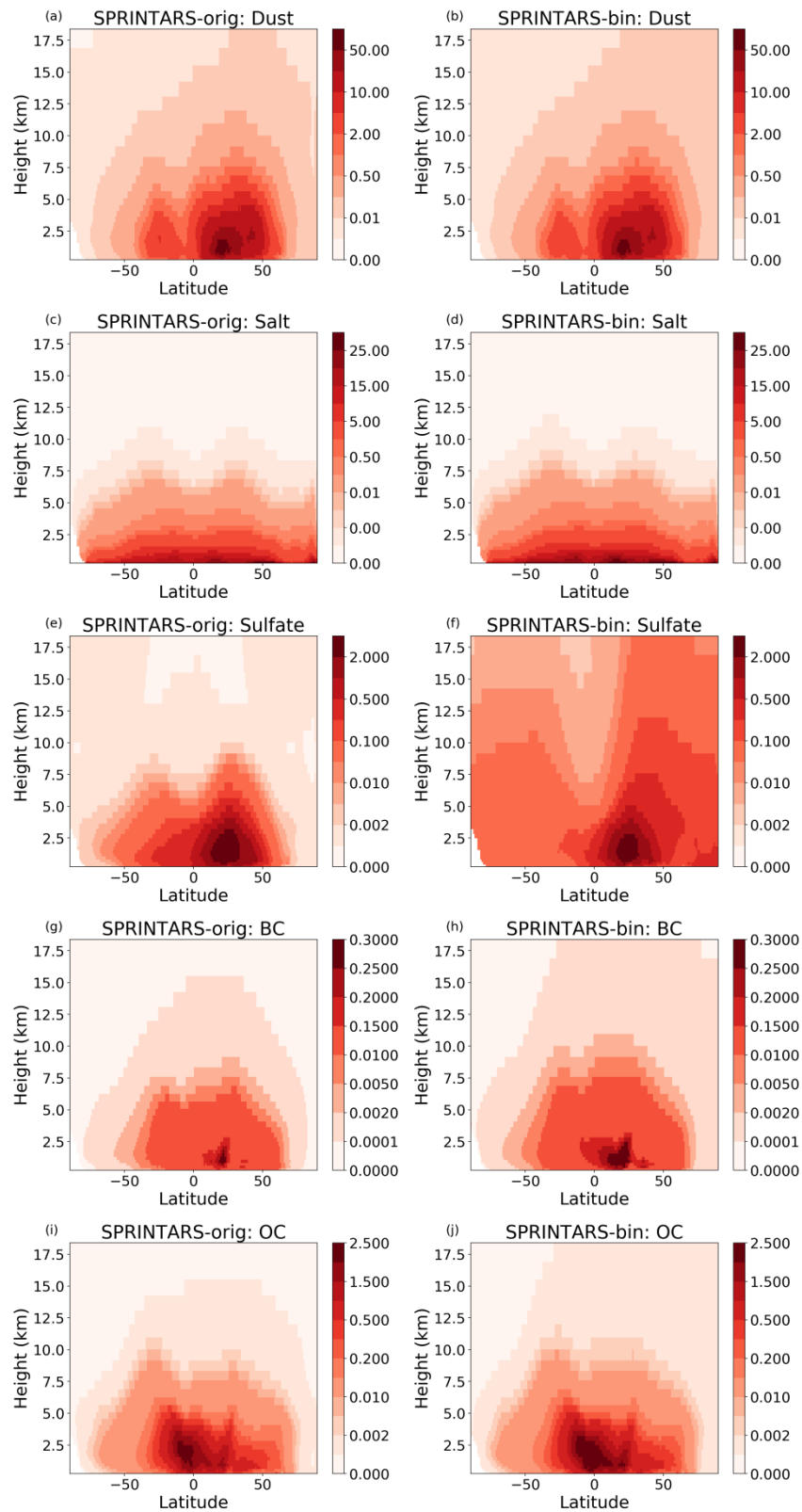
Fig. 4 Annually-average, the zonal-mean vertical profile of the mass concentrations

(μg m^{-3}) of each aerosol type predicted by the original and sectional models.
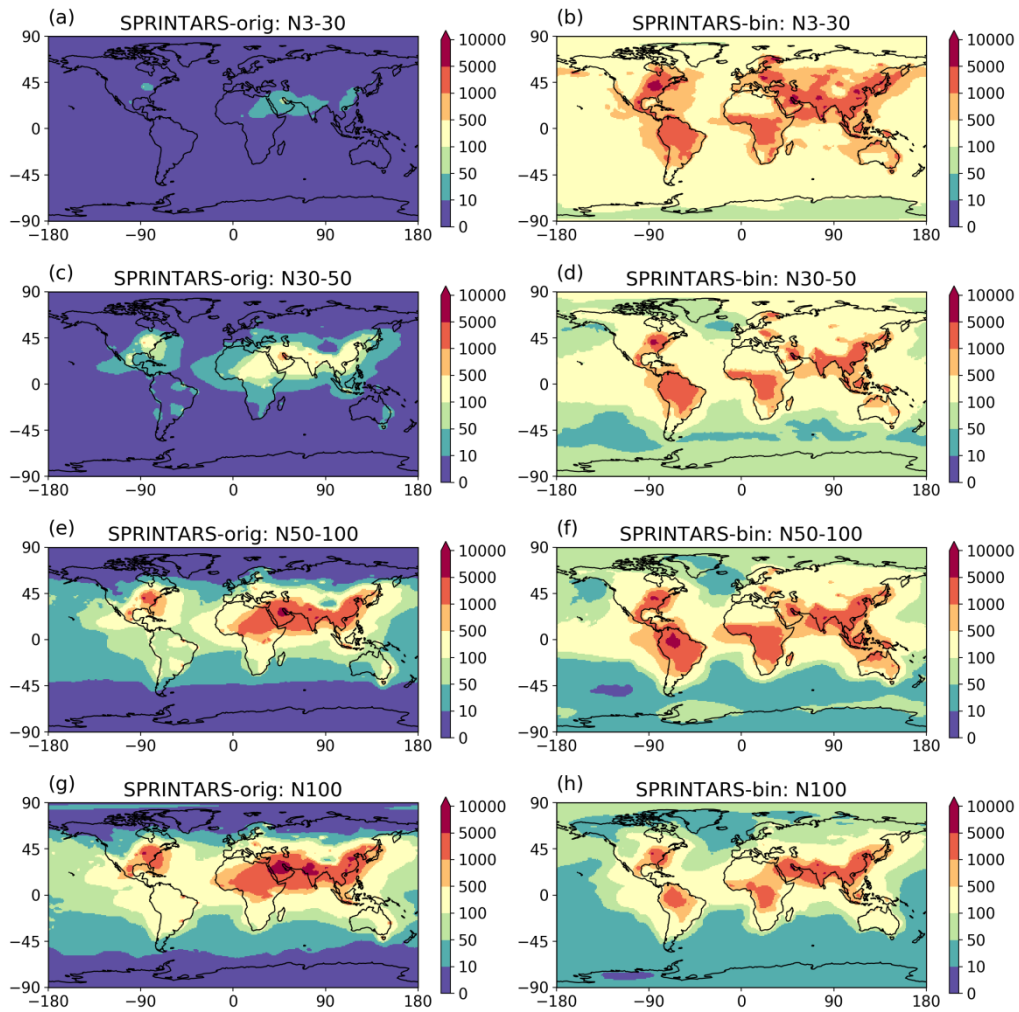
1344

Fig. 5   Annually-averages of the surface number concentrations (cm^{-3}) of total aerosols, divided into 4 size classes, each representing the total number of particles with dry diameters (a)& (b) between 3 to 30 nm; (c) & (d) between 30 to 50 nm; (e) & (f) between 50 to 100 nm; (g) & (h) larger than 100 nm.

1349

1350

1351

1352

1353

(a) 3-30 nm

(b) 30-50 nm

(c) 50-100 nm

(d) 100-700 nm

(e) 700-1000 nm

(f) >1000 nm
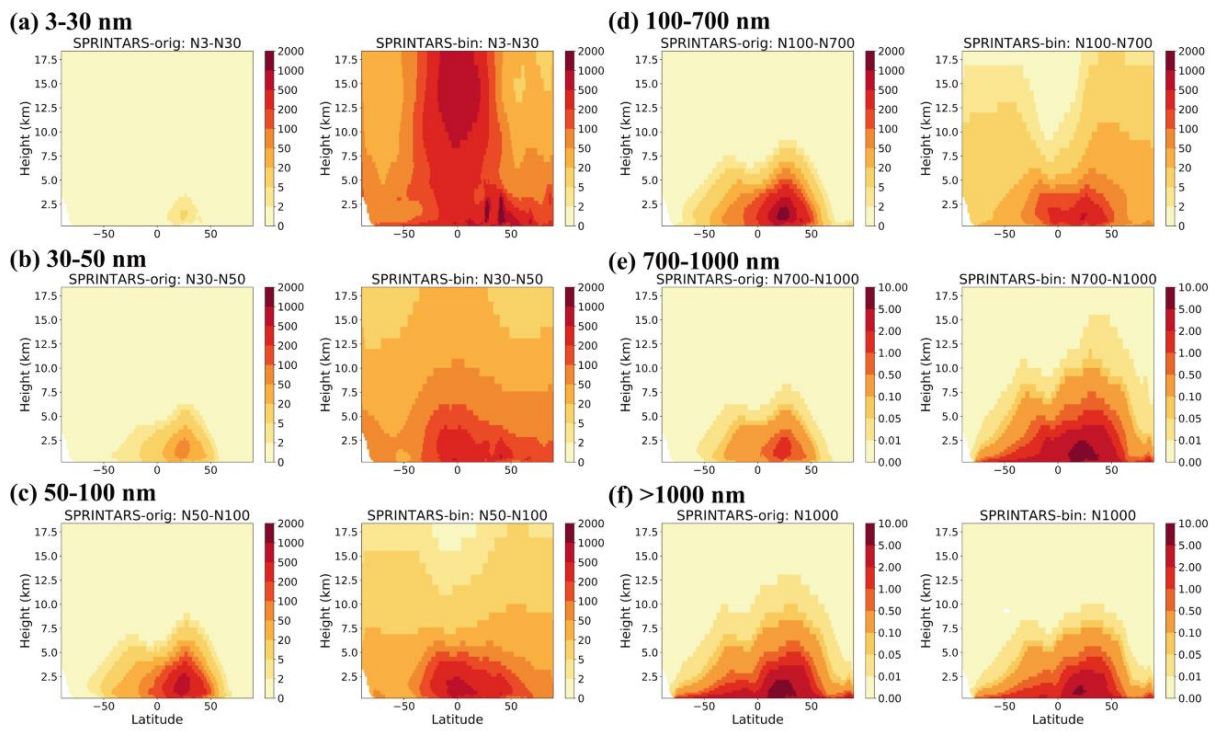
1354

Fig. 6   Annually-averaged, the zonal-mean vertical profile of number concentrations (cm^{-3}) of particles with dry diameters (a) between 3 to 30 nm, (b) between 30 to 50 nm, (c) between 50 to 100 nm, (d) between 100 to 700 nm, (e) between 700 to 1000 nm, and (f) larger than 1000 nm.

1355

1356

1357

1358

1359

1360

1361
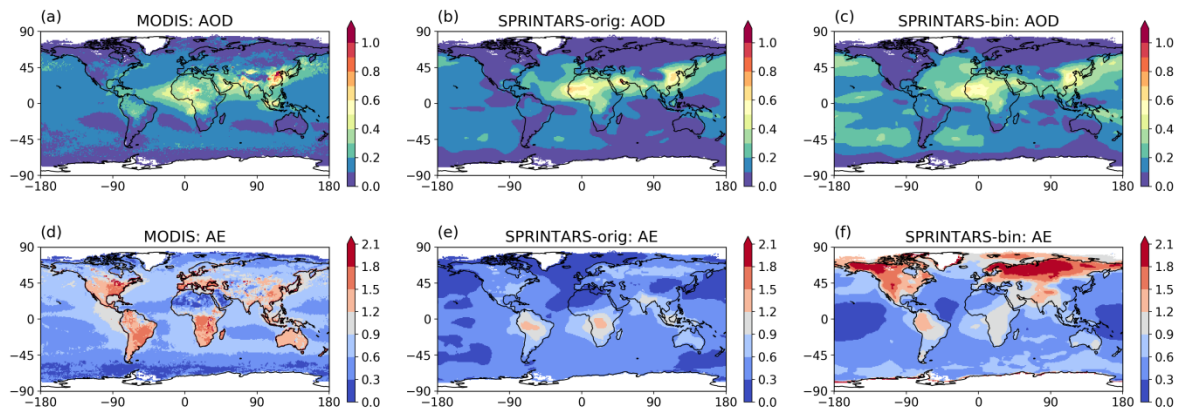
1362

Fig. 7   Distributions of annually-averaged (a-c) aerosol optical depth (AOD) and (d-f)

Angstrom Exponent (AE), observed by (a & d) MODIS and predicted by (b & e)

NICAM-SPRINTARS-orig and (c & f) NICAM-SPRINTARS-bin.

1363

1364

1365

1366

1367

1368
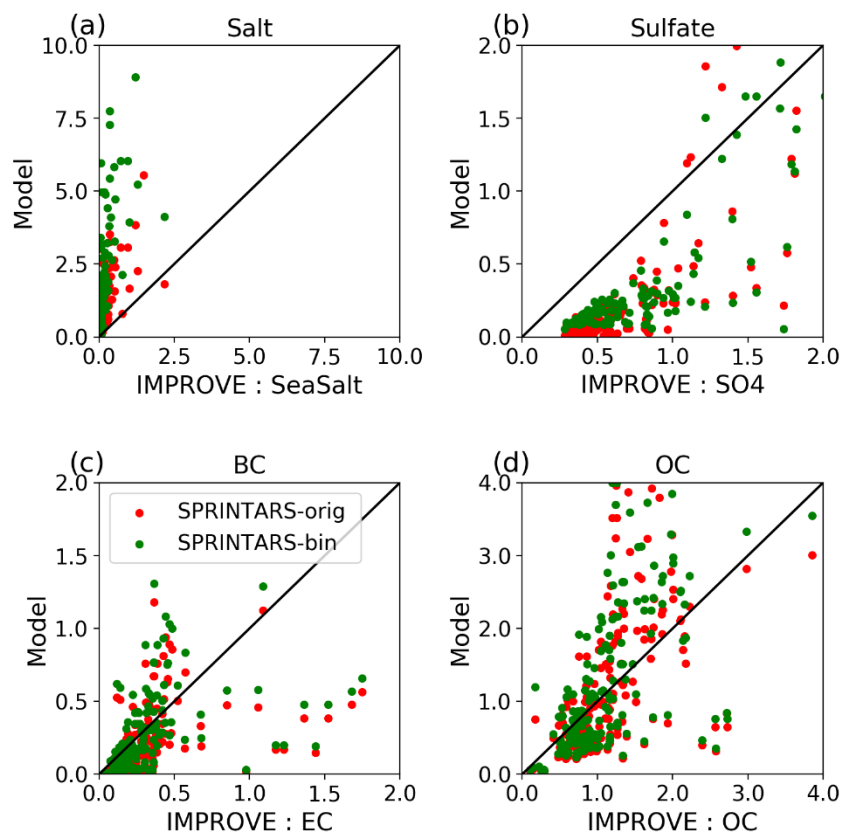
1369

Fig. 8   Scatter plots of the annual averages of surface mass concentrations of (a) sea salt, (b) sulfate, (c) elemental carbon (black carbon), and (d) OC at the IMPROVE stations. Simulations results by NICAM-SPRINTARS-orig and NICAM-SPRINTARS-bin are represented by red and green dots, respectively. Only fine particles (diameter < 2.5 μm) are considered.
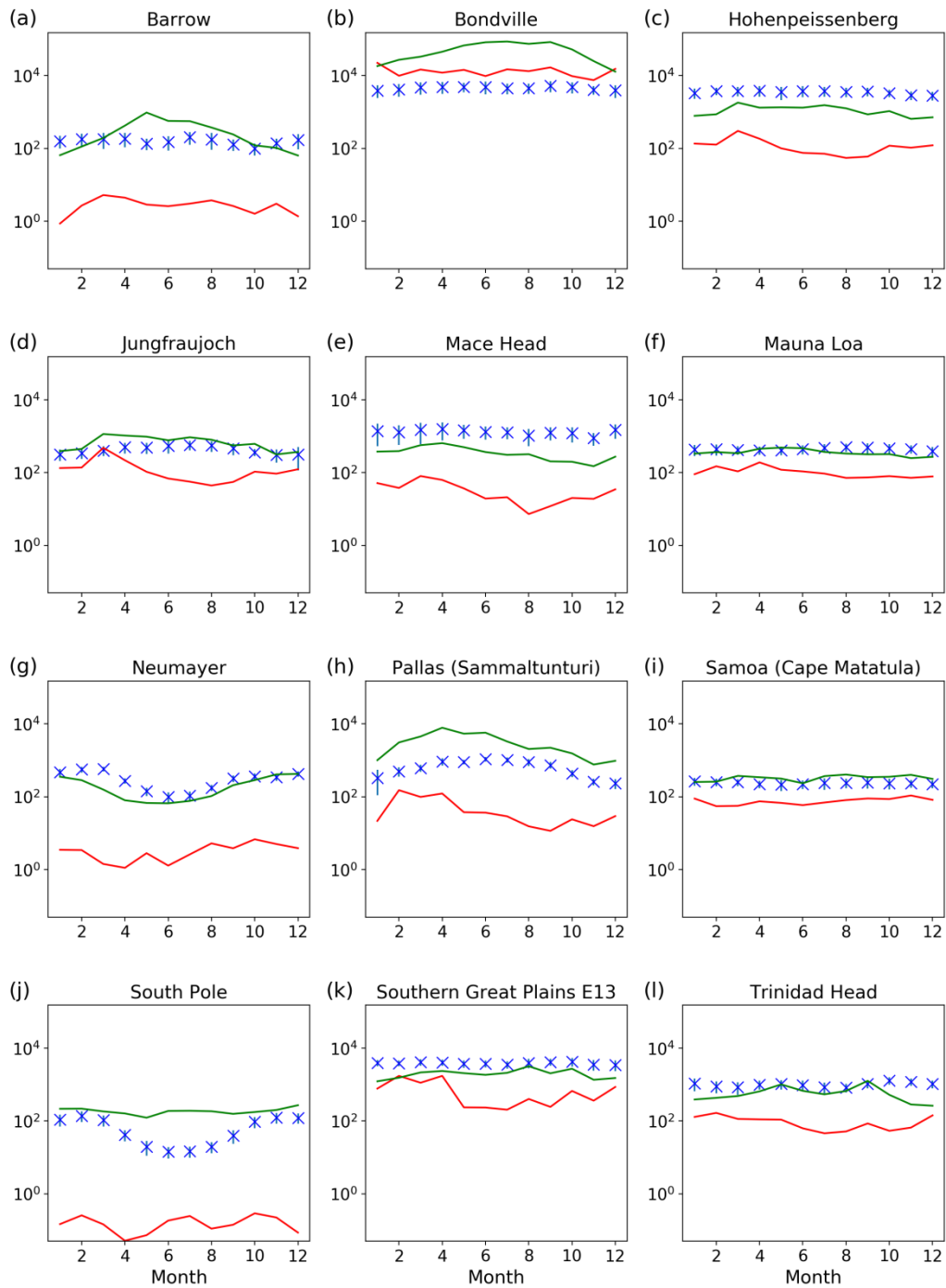
1370
1371
1372
1373
1374

1375
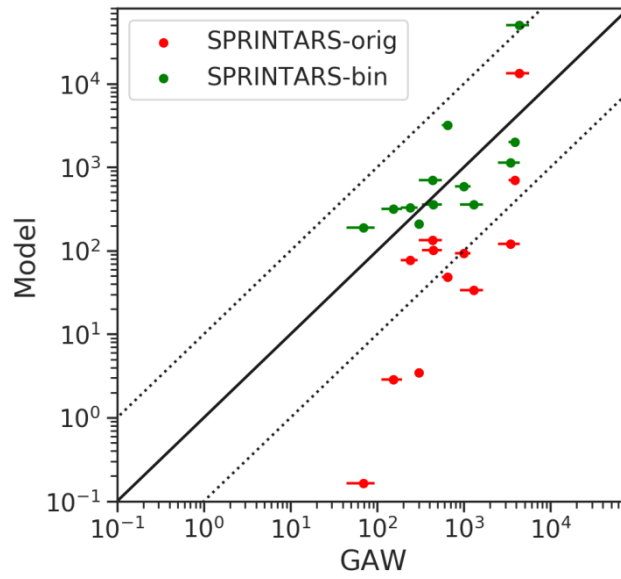
1376

Fig. 9   Scatter plot of the annual averages of the total number concentrations at
GAW stations. The dotted lines indicate the range of model-observation values
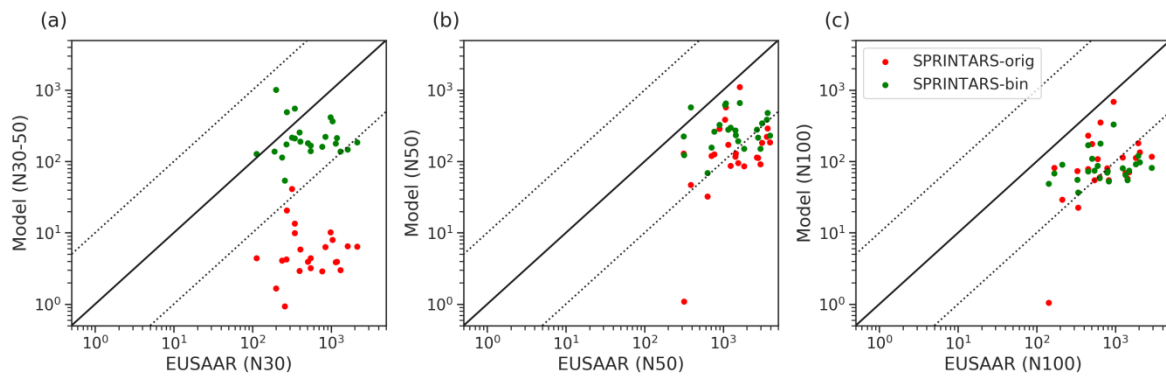within one order of magnitude.

1380

Fig. 10 Monthly averages of the total number concentrations at each of the GAW stations. Blue markers represent the multi-year averages, with the vertical bars indicating one standard deviation. Red and green lines show the results by the original and sectional model.
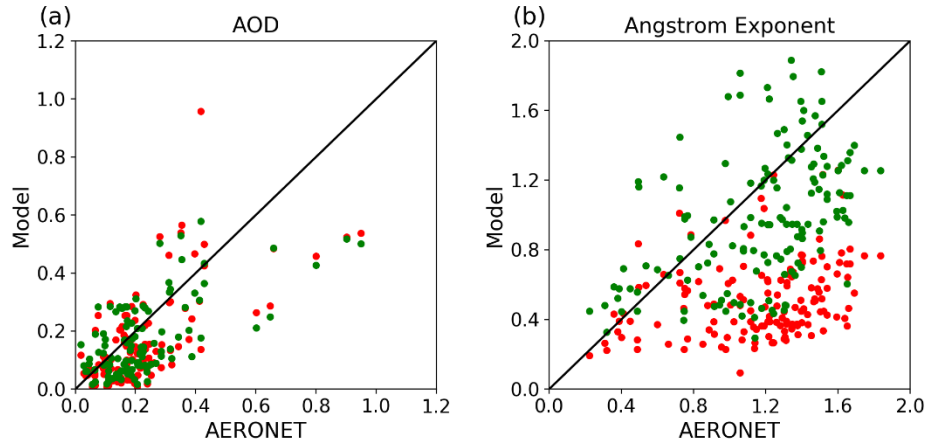
1387

1388 Fig. 11　Scatter plots of the annual averages of number concentrations of particles

1389 with dry diameters (a) between 30 and 50 nm (N30-50), (b) larger than 50 nm (N50)

1390 and (c) larger than 100 nm (N100), against the measured values at EUSAAR

1391 stations during 2008-2009.

1392

1393

Fig. 12   Scatter plots of annual averages of AOD (550 nm for model results; 500 nm for AERONET) and Angstrom Exponent (440 nm and 870 nm) predicted by both models against the observed values at AERONET stations. Red and green markers represent the values by NICAM-SPRINTARS-orig and NICAM-SPRINTARS-bin, respectively.

1399

1400

1401

1402

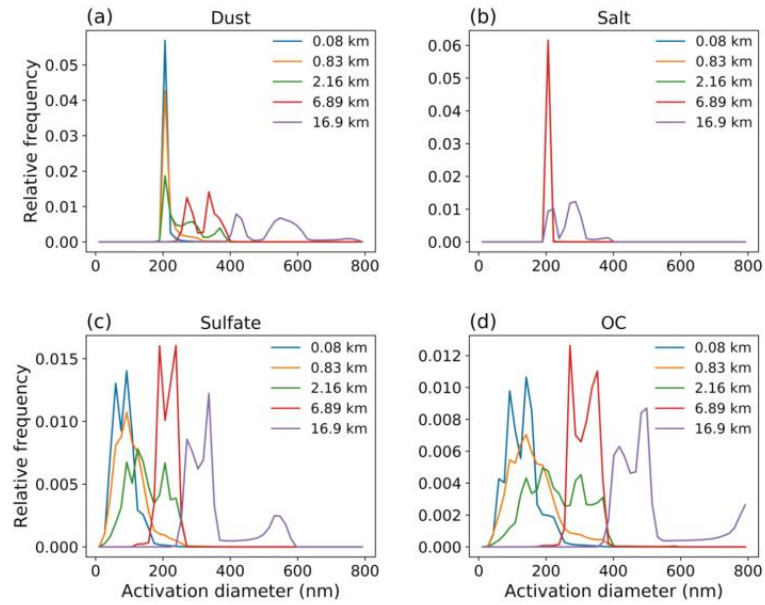1403

1404

1405

1406

Fig. 13   Histogram of the activation diameters of different aerosol types at certain heights, calculated using a combined scheme of Abdul-Razzak & Ghan, 2000 & 2002. A total of 23,652,000 valid points are considered in each histogram, covering the daily 1°x1° output. The results of black carbon are not presented due to the large uncertainties in hygroscopicity.

1416   List of Tables

1420

1421　Table 1　　Size representations in SPRINTARS-orig and SPRINTARS-bin. The modal

1422　diameters refer to the dry mode diameters of the assumed number distributions. Modal

1423　diameters and size ranges are expressed in μm.

	SPRINTARS-orig				SPRINTARS-bin	
	Modal diameter	Modal width	Range	Bin number	Range	Bin number
Sea salt	-	-	0.2-20	4	0.2-20	20
Dust	-	-	0.2-20	10	0.2-20	20
Sulfate	0.139	2.03	-	-	0.003-10	20
Carbonaceous aerosols						
OC	0.2	1.8	-	-		
BC	0.1076	1.53	-	-	0.08-5.0	20
BSOA	0.16	1.8	-	-		

1424

1425

1426 Table 2 Correlation and bias (averaged relative error) of the model estimates against
1427 ground-based measurements. IMPROVE: Surface mass concentrations; GAW: Total
1428 number concentrations; EUSAAR: Number concentrations (num. conc.) in size classes;
1429 AERONET: AOD and Angstrom Exponent. The correlation and bias of number
1430 concentrations are calculated in logarithmic scale.

	NICAM-SPRINTARS-orig		NICAM-SPRINTARS-bin	
	Correlation	Bias	Correlation	Bias
IMPROVE				
Sea salt (fine)	0.68	5.79	0.69	14.2
Sulfate	0.73	-0.22	0.65	-0.29
Elemental carbon	0.45	-0.33	0.45	-0.15
Organic carbon	0.53	-0.01	0.53	-0.16
GAW				
Total number concentration	0.84	-0.45	0.71	0.04
EUSAAR				
Num. conc. ($30nm \leq d < 50nm$)	0.26	-0.79	-0.01	-0.13
Num. conc. ($d \geq 50nm$)	0.46	-0.34	0.15	-0.22
Num. conc. ($d \geq 100nm$)	0.50	-0.34	0.23	-0.32
AERONET				
Aerosol optical depth	0.65	-0.16	0.64	-0.05
Angstrom Exponent	0.29	-0.50	0.45	-0.10

1431

1432